Pre-Shower Detector and Particle Identification at sPHENIX

Kazuya Nagashima
(M131852)

Quark Physics Laboratory
Department of Physics
Graduate School of Science
Hiroshima University

Supervisor	:	Associate Prof.	Kenta Shigaki
Primary examiner	:	Associate Prof.	Kenta Shigaki
Examiner	:	Prof.	Yasushi Fukazawa

February 23, 2015

Abstract

A new state of matter called Quark Gluon Plasma (QGP) existed within 10 microseconds after the big bang. QCD has the property of asymptotic freedom which is decreasing running coupling constant (α_s) with increasing momentum transfer, and causes a phase transition to QGP under conditions of extreme temperature and net baryon density. We plan sPHENIX, the upgrade of PHENIX (the Pioneering High Energy Nuclear Interaction eXpariment) for a perfect solution of physics properties of QGP. In this thesis, the design of the Pre-Shower detector and the particle identification at sPHENIX are studied.
(1) Design of the Pre-Shower detector
The Pre-Shower detector can detect the early stage of electromagnetic showers, and identify particles. The main motivation of the Pre-Shower is to separate direct photons produced in the initial hard scattering from background photons having very narrow opening angles from decays of neutral mesons at high transverse momenta. At the leading order, photons are produced back-to-back with the same transverse energy of associated partons (Jets). Therefore the energy loss of partons in the hot and dense medium can be measured via the transverse momentum ratio of direct photons and jets, because photons do not strongly interact. In this thesis, the size of silicon pad and the thickness of the Pb convertor were decided on the basis of signal-to-noise ratio of direct photons. In a single particle simulation, the ratio of direct photons to neutral π meson can be improved be up to a factor of 6 times.
(2) Particle Identification at sPHENIX
The yields of upsilon meson states are suppressed sequentially by QCD debye screening in a hot and dense medium, because the effect of QCD debye screening depends on the distance between the two quarks. Therefore the relationship between the physical size of quarkonia and QCD debye screening can be solved via the measuremnt. The signal-to-background ratio and the statistics are both critical for a successful measurement of the upsilon meson states. In this thesis, the method of electron identification is established, and the charged hadron rejection is evaluated to be over 100. In this condition, the signal-to-background of invariant mass spectram of upsilon meson states is above the unity.

Contents

List of Figures

1 Introduction

1.1 Modern Particle Physics

1.1.1 Standard Model

The Standard Model of particle physics is a theory concerning the electromagnetic, weak and strong nuclear interactions which mediate the dynamics of the known subatomic particles. At the Standard Model, seventeen elemental particles and three fundamental interactions are assumed. twelve out of elemental particles are a matter particles called quarks and leptons, the others are defined as force carriers that are called gauge particles included Higgs particle which gives a mass to elemental particles, W and Z bosons.

1.1.2 Quantum Electro-Weak Dynamics

The electromagnetic interaction is described by Quantum Electro Dynamics (QED) as a relativistic quantum field theory. A photon of a gauge boson mediates the electromagnetic interaction. Many theoretical values of QED agree with experimental values in a high accuracy. The Lagrangian of QED is expressed by a following formula.

$$L_{QED} = \sum_f \overline{\psi}_f (i\gamma^\mu \partial_\mu - m_f)\psi_f + e\sum_f Q_f \overline{\psi}_f \gamma^\mu \psi_f A_\mu - \frac{1}{4} F_{\mu\nu} F^{\mu\nu} \tag{1}$$

Here, ψ_f is the spinor which is wave function of spin, γ^μ is Dirac matrix, Q_f is elementary charge, A_μ is electromagnetic vector potential, shows photon field, $F_{\mu\nu}$ is electromagnetic tensor. The second item of the Lagrangian shows interaction between charged particles and electromagnetic field. That means the probability amplitude is in proportion to eQ_f. Also the weak interaction causes beta decay by mediating W and Z bosons. Today electromagnetic and weak interactions are unified by the Weinberg-Salam theory and called the electro-weak interaction.

1.1.3 Quantum Chromo Dynamics

Quantum Chromo Dynamics (QCD) describes the strong interaction of quarks and gluons with color charge exchange. Gluon of a gauge boson mediates the strong interaction. The QCD was developed as an extension of QED via the imposition of a local SU(3) symmetry in color space and based on the gauge field theory. Its lagrangian is expressed by a following formula.

$$L_{QCD} = \sum_q \overline{\psi}_{q,a} (i\gamma^\mu \partial_\mu - m_q)\psi_{q,a} + g_s \sum_q \overline{\psi}_f \gamma^\mu T^A_{ab} \psi_{q,b} G^A_\mu - \frac{1}{4} G^A_{\mu\nu} F^{A\mu\nu} \tag{2}$$

L_{QCD} and L_{QED} are in the same form. $\psi_{\mathrm{q,a}}$ is the quark field, g_s is the coupling constant of QCD, G^A_μ is the tensor of gluon field, T^A is the generator matrix of SU(3). L_{QCD} is remained invariable with gauge transformation. A feature of QCD is the momentum transfer dependence of the strong coupling constant α_s that is expressed in the following.

$$\alpha_s(\mu_R^2) \simeq \frac{1}{b_0 log(\mu_R^2/\Lambda_Q^2 CD)} = \frac{12\pi}{(33-2n_q) log(\mu_R^2/\Lambda_Q^2 CD)} \tag{3}$$

Here, Λ_{QCD} is the scale parameter of the strong interaction ($\Lambda_{QCD} \simeq 200$MeV) and n_f is the number of active quark flavors with quark mass less than Q. Figure 1 shows the running coupling constant as a function of the momentum transfer. As shown in Figure 1, in case of a large momentum transfer and equivalently at a short distance, the α_s decreases logarithmically, and quarks and gluons are freed from confined state. This phenomenon is produced with asymptotic freedom caused by non-commutative gauge theory of QCD.

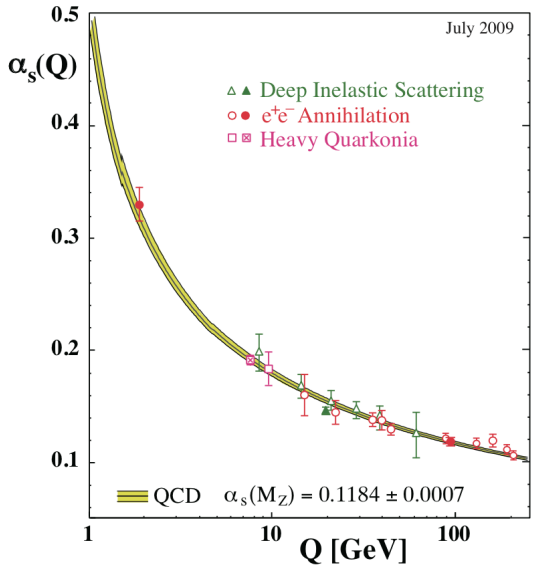

Figure 1: Running coupling constant α_s of strong interaction of a function of the momentum transfer, Q [1]

1.1.4 Quark Gluon Plasma

A new state of matter called Quark Gluon Plasma (QGP) existed within 10 microseconds after the big bang. QCD has the property of asymptotic freedom which express decreasing the running coupling constant (α_s) with increasing momentum transfer, and causes a phase transition to QGP under conditions of extreme temperature and net baryon density. That is to say, quarks are released from confined state with increasing energy scale (> 200 MeV, > 2 GeV/fm^3). Figure 2 shows a theoretical phase diagram of nuclear matter as a function of baryo-chemical potential μ and temperature T. QGP phase is created by high energy heavy ion collisions. In recent years, QGP was measured as nearly perfect fluid which was contrary to expectations by Relativistic Heavy-Ion Collision (RHIC).

1.1.5 Relativistic Heavy-Ion Collision (RHIC)

High energy heavy-ion collision is the only way to create QGP phase. It is performed with Relativistic Heavy-Ion Collision (RHIC) at Brookhaven National Laboratory (BNL). RHIC can accelerate a variety of nuclear beams from protons (p) to gold ions (Au) with maximum energy up to 500 GeV for p and 200GeV per nucleon for Au. At first stage of acceleration, p and Au, are produced and accelerated by the Linac and the Tandem

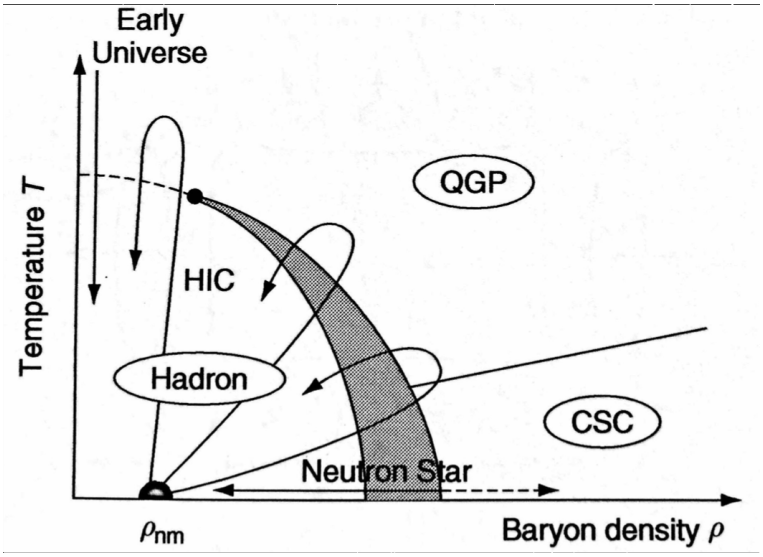

Figure 2: QCD phase diagram [2]

Van de Graaff pre-accelerator. Secondly, the produced beam is more accelerated by the Alternating Gradient Synchrotron (AGS). AGS can accelerate the beam unto 28 GeV for p and 10.8 GeV for Au per nucleon, and send into the RHIC rings. Finally, the beams are accelerated up to its maximum energy and collided.

1.1.6 Time Evolution

At high energy heavy-ion collision, the ion is accelerated nearly to the speed of light. At this time, it is disk shape by Lorentz contraction and the Color Glass Condense (CGC) that is saturation of gluon in atomic. At collision, part of partons scatter with large momentum transfer in hard processes over very short time scales, τ ($1/p_T < 0.1$fm/c). On the other hands, most of the quarks pass through and interacted gluons create Glasma that is gluon plasma. Quark pairs are created by gluon fusion in glasma. And then quarks and gluons become local equilibration that is occurring QGP phase transition. Temperature of QGP decrease with quickly expansion, quarks and gluons are recombined and create hadron gas phase. It is become final state with through chemical freeze-out and thermal freeze-out.

1.2 Past Results at RHIC and LHC

1.2.1 High Transverse Momentum Suppression

High p_T particles are produced by heavy ion collisions and loss energy when pass through the matter created in the collision. The mechanism of energy loss in the dense matter is thought to be the gluon bremsstrahlung radiations and parton elastic scatterings. This effect can be measured with the nuclear modification factor.

$$R_{AB} = \frac{dN^2_{AB}/dydp_T}{(< N_{coll} > /\sigma^{inel}_{pp}) \times d^2\sigma_{pp}/dp_T} \quad (4)$$

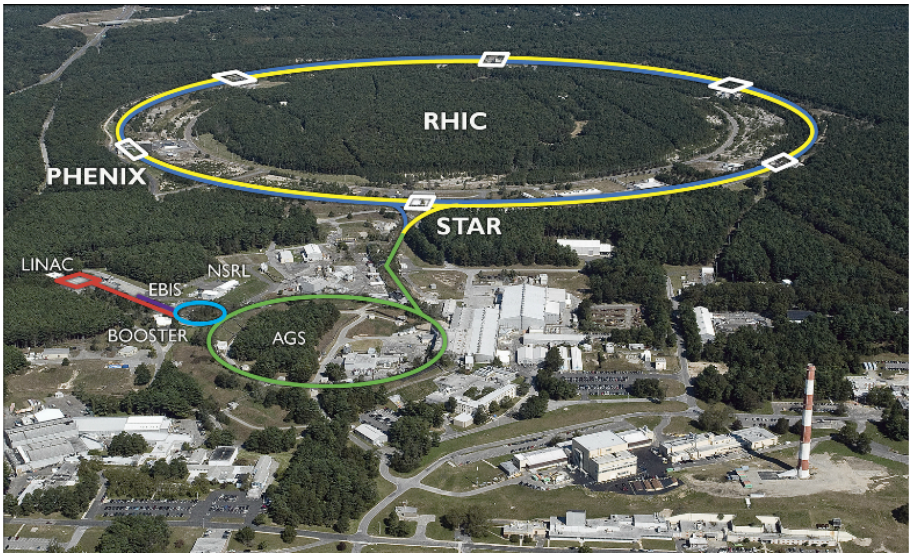

Figure 3: Relativistic Heavy Ion Collider (RHIC) of the BNL [3]

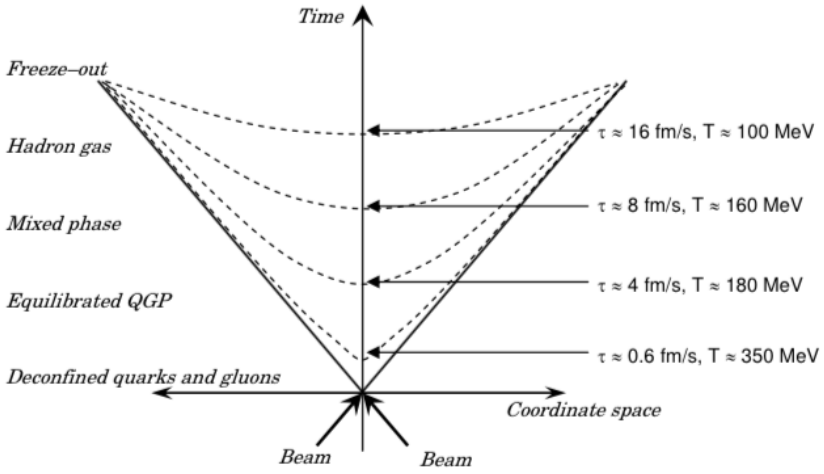

Figure 4: The space time evolution in heavy ion collisions. [4]

where $d^2N_{AA}/\mathrm{dyd}p_T$ is the invariant yield per unit rapidity, N_{coll} is the number of binary heavy-ion collision on the impact parameter range of corresponding centrality, σ_{pp} is the cross section for inelastic proton-proton collisions. Figure 5 shows the nuclear modification factor each particles. If medium effect do not exit, π^0 and η R_{AA} should be 1. But practically yield of π^0 and η decrease greatly at high p_T. On the other hands, direct γ R_{AA} is $R_{AA} = 1$ because of not interacting strongly in a medium. So R_{AA} describes the effect of energy loss in a medium by strong interaction.

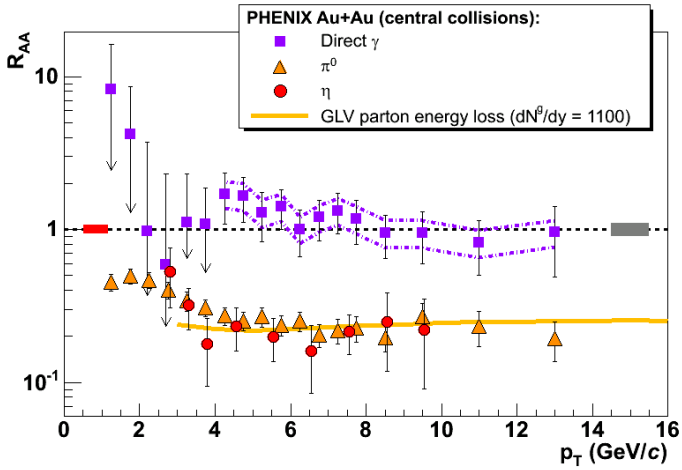

Figure 5: Neutral pi meson (π^0) (yellow), eta meson (η) (red) and direct γ (purple) R_{AA} as a function of transverse momentum for central Au + Au collisions. [5]

1.2.2 Jet Quenching

The production time scale of high p_T partons and photons in pQCD processes are very short, $\tau < 1/p_T < 0.1$ fm/c. Thus their yields can be modified by interact on with medium. The back-to-back dijets are produced by the pQCD process, which have same transverse energy. So transverse momentum unbalance can be used as probes to study the strongly interacting medium created, because these unbalances are occurred by difference of medium pass length on the right plot in Figure 6. The left plot in Figure 6 show di-hadron correlations as measured by RHIC. The horizontal axis is the angle between the leading and the subleading particle. The away side peak is clearly visible in p+p and d+Au collisions, but is absent in Au+Au collisions. This is jet quenching by interactions in the medium.

1.2.3 Heavy Flavor

The mechanism of parton energy loss is gluon radiation and elastic scattering in QGP. Quark dE/E depends on quarks mass. Especially bottom quark dE/E is extremely smaller than others. Today, the energy loss of hadron including u, d and c quarks were measured, but b did not. So B meson including bottom quark should be measured for effect of energy loss in pp and AA collisions. Separating c/b quark is difficult to achieve with semi-leptonic channel because of the single lepton spectrum contains both charm and bottom contributions. So it is challenges for the future.

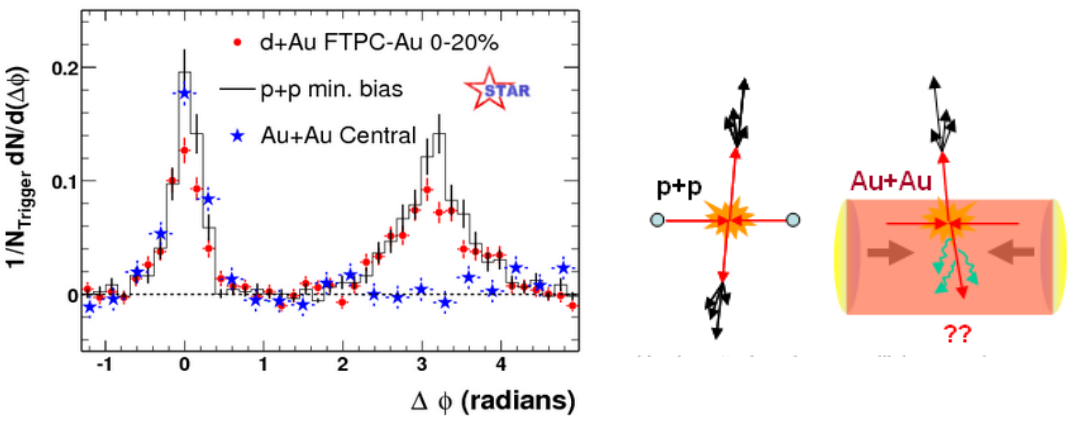

Figure 6: Di-hadron correlations as measured by RHIC. The horizontal axis is the angle between the leading and the subleading particle. [6]

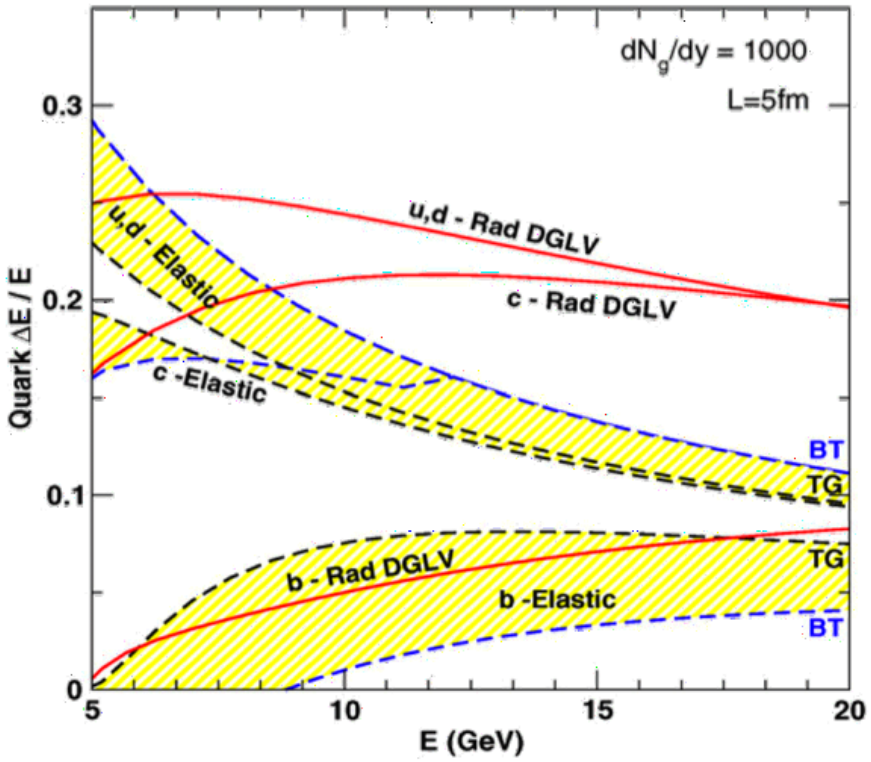

Figure 7: Comparison of the average radiative and elastic energy losses of light and heavy quarks passing through the medium produced in central AuAu collisions at RHIC energies [7]

1.2.4 Heavy quarkonia

$c\bar{c}$ and $b\bar{b}$ vector masons are called the quarkonia (i.e. J/ψ, Υ and so on). These are produced by only hard-scattering in nucleons-nucleons collisions, and affected by the QCD debye screening which is break bound state of quarks by color charged particles in the hot and dense medium. Especially, the yields of upsilon meson states are suppressed sequentially by QCD debye screening in a hot and dense medium, because the effect of QCD debye screening depends on the distance between the two quarks. Therefore the relationship between the physical size of quarkonia and QCD debye screening can be solved via the measuremnt. Figure 8 shows the mass distribution of upsilon three states in PbPb $\sqrt{S_{NN}} = 2.76$ TeV.

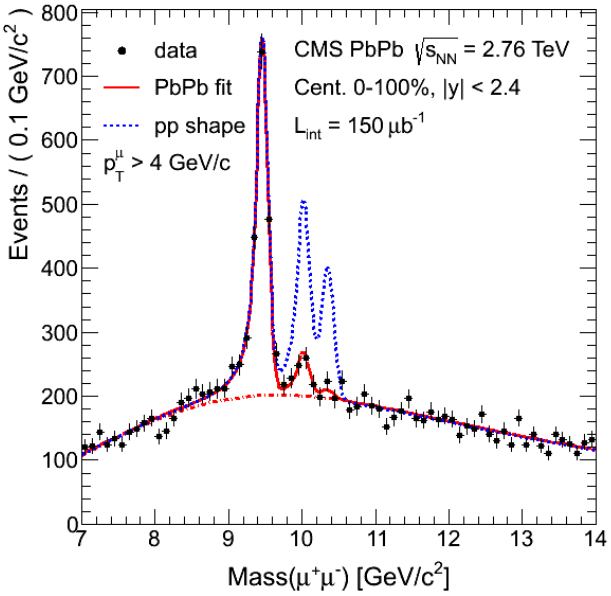

Figure 8: The mass spectrums measured with CMS are compared between in pp and Pb+Pb. [8]

1.3 Motivation of this thesis

We plan sPHENIX, the upgrade of PHENIX (the Pioneering High Energy Nuclear Interaction eXpariment) for a perfect solution of physics properties of QGP. The sPHENIX detector will be able to measure jets, b-tagged jets, photons, heavy flavors, quarkonia with a wide energy range. In this thesis, I focus on measurement of photons, heavy flavor and quarkonia.

Firstly, I studied the design of the Pre-Shower detector for separating direct photons from decay photons. Figure 9 show the count/event of direct photon and π^0 at RHIC and LHC, and these ratio. In case of RHIC, the ratio of direct photons to π^0 is larger than three in the region of 25 GeV $\leq p_T$. In the p_T region from 10 to 25 GeV/c, however, direct photons cannot be tagged or measured due to overwhelming decay photons as the electromagnetic calorimeter can identify photons from π^0 only up to 10 GeV/c. So we proposed Pre-Shower detector which fills the gap of single photon measurement, and extends the

direct photon tagging to the lower transverse momentum. The performance goal is to improve the signal-to-background ratio by a factor 3.
Secondly, I studied the identification of electron for measurements of upsilon 3 states, where the signal-to-background ratio and the statistics are both critical for a successful measurement. Figure 10 show the upsilon mass distribution before and after subtracting background under condition of a pion rejection factor of 90% and a pair identification efficiency of 49 %. So I established the method of identifying electrons using the sPHENIX detectors for the measurement and evaluated pion rejection which is the ratio of electron efficiency to charged pion efficiency.

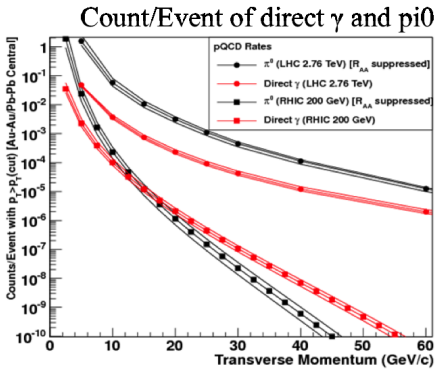

[1] count

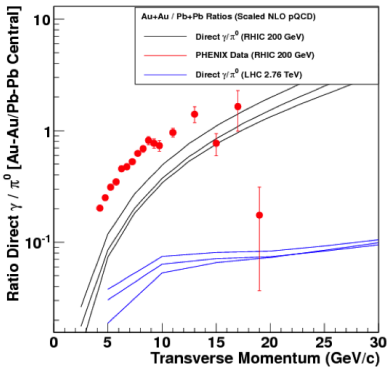

[2] ratio

Figure 9: NLO pQCD calculations of direct photons and π^0 for RHIC and LHC. The counts per event in Au+Au or Pb+Pb collisions on the left plot. The direct photon to π^0 ratio in p+p (Au+Au or Pb+Pb) on the right plot. [9]

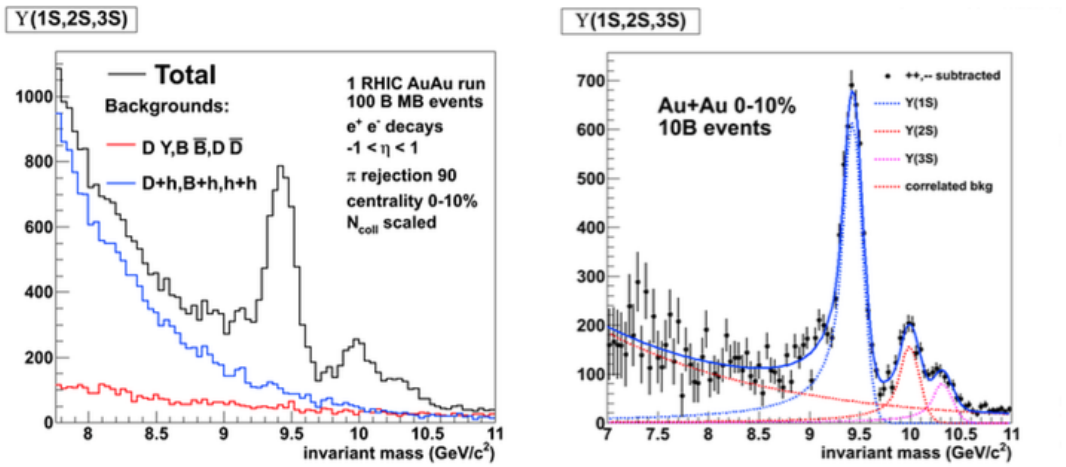

Figure 10: (Left)The signal plus background in the Upsilon mass region for ten billion 0-10 % central Au+Au events, assuming a pion rejection factor of 90, with the signal reduced by a pair identification efficiency of 49 %. The combined backgrounds due to correlated bottom, correlated charm, and Drell-Yan are shown as the red curve. The combined backgrounds due to fake electrons combining with themselves, bottom, and charm are shown as the blue line. (Right) The expected invariant mass distribution for ten billion 0-10 % central Au+Au events, after subtraction of combinatorial background using the like-sign method. [9]

2 sPHENIX Experiment

The sPHENIX is a major upgrade to the PHENIX detector at the Relativistic Heavy Ion Collider. The physics programs of sPHENIX primarily aim at jets and heavy flavors addressing fundamental questions about the nature of the strongly coupled quark-gluon plasma. We have a run plan for 2021-2022 including of 22 weeks of Au+Au, and extended periods of p+p and p(d)+Au running with the high luminosity available at RHIC and the high data acquisitions bandwidth at sPHENIX. sPHENIX will record 100 billion and sample over 2/3 of a trillion Au+Au collision at $\sqrt{S_{NN}} = 200$ GeV.

2.1 Physics Motivation

The physics cases for sPHENIX are in the following.
1. Jets, Heavy Quark jets
The energy loss of a parton and the parton shower evolving in medium are understood via the measurement of jets. Theoretical calculations attempting to describe the wealth of new data from RHIC and the LHC have not yet reconciled some of the basic features, with some models including large energy transfer to the medium as heat and others with mostly radiative energy loss. Figure 12 shows the produceted diet asymmetry (A_j) at RHIC for mid-central and central Au+Au collisions for leading jets $E_{T1} > 20$ GeV and jet radius parameter $R = 0.4$ and $R = 0.2$ in the left and right histograms. The diet asymmetry is expressed $A_j = (E_1\text{-}E_2)/(E_1+E_2)$.

2. Direct Photons and Fragmentation Functions

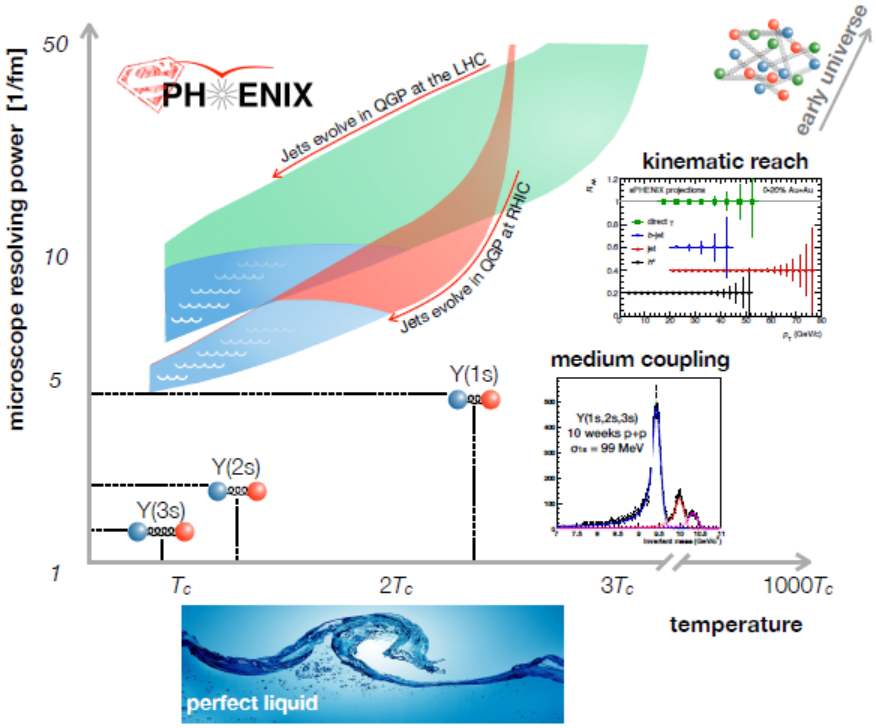

Figure 11: The physics goals of sPHENX [9]

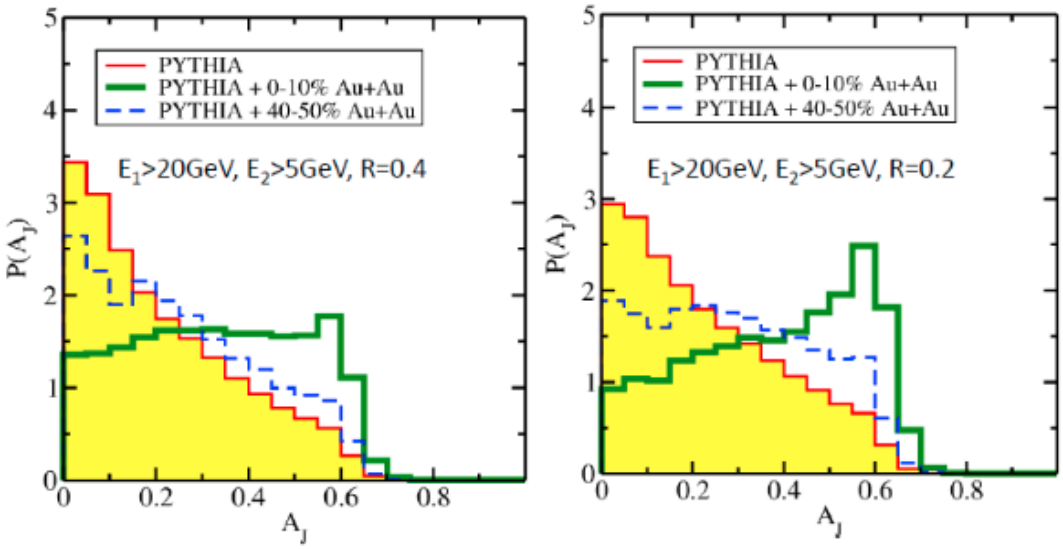

Figure 12: Calculasion results of dijet A_j. Central (green) and mid-central (blue) distributions are shown along with the initial PYTHIA(a widely used pQCD event generator) distributions (red). [9]

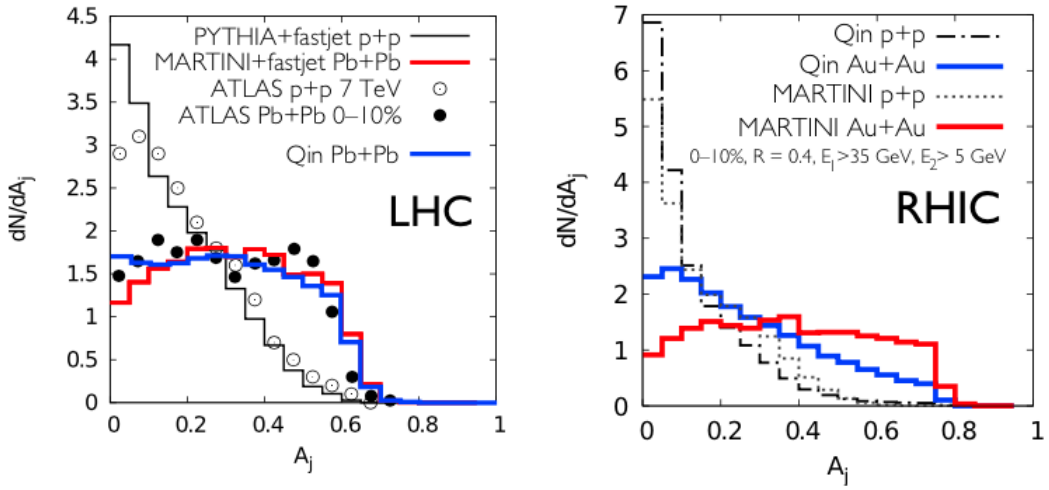

Figure 13: Calculation results for the vacuum and medium modified distribution for direct photon-reconstructed jet event at LHC collision energy (left) and RHIC collision energy (right) [9]

At leading order (LO), photons are produced with the same transverse energy of associated partons. Therefore the energy loss of partons in the hot and dense medium can be measured with the transverse momentum ratio of direct photons and jets, because photons do not strongly interact. In other wards, photon + jet productions are the " golden channel " to investigate energy loss of partons in the medium. Figure 13 shows the ratio of the reconstructed jet energy with $R = 0.3$ relateve to the direct photon energy. Here, $z_{j\gamma}$ is expressed $z_{j\gamma} = p_T^{jet}/p_T^{\gamma}$.

3. Beauty Quarkonia in the QGP

The yields of upsilon meson states are suppressed sequentially by QCD debye screening in a hot and dense medium, because the effect of QCD debye screening depends on the distance between the two quarks. Therefore the relationship between the physical size of quarkonia and QCD debye screening can be solved via the measurements. And the temperature dependency of QCD debye screening can be measured with comparison between RHIC and LHC. Figure 14 shows the reconstructed mass spectrum for dielectric decays with simulation at sPHENIX.

2.2 sPHENIX Detectors

The sPHENIX detectors include the silicon tracking, electromagnetic and hadronic calorimeters, magnetic solenoid and readout electronics. The sPHENIX is large acceptance (ϕ=2π,η= $\pm$ 1.1) and 15k Hz data acquisition. Detectors performance are studied using a full GEANT4 simulation of the detector. The sPHENIX detectors will be able to measure jets, b-tagged jets, photons, quarkonia, charged hadron with a wide energy range.

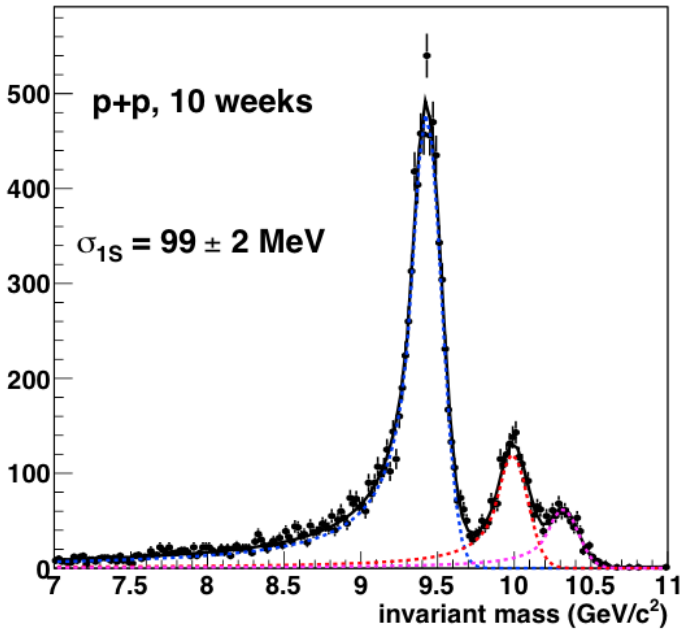

Figure 14: The mass spectrum from reconstructed electron decay tracks for the three Upsilon states. [9]

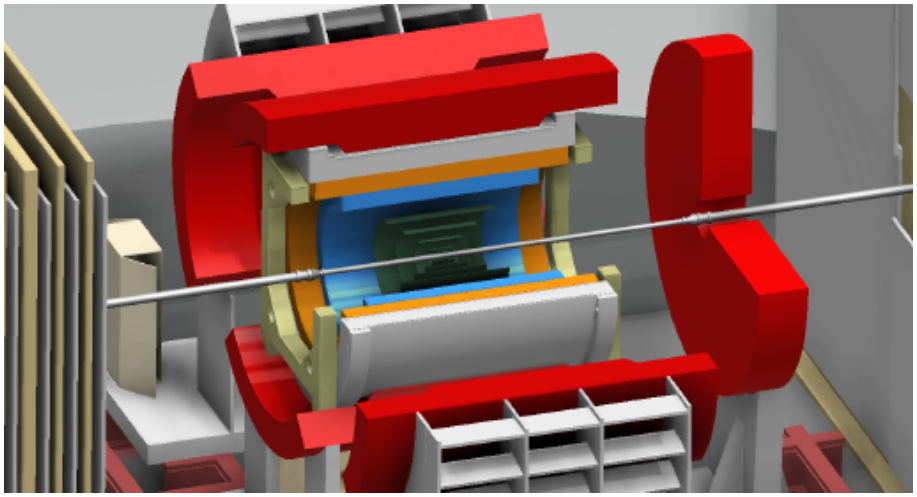

Figure 15: sPHENIX detectors. [9]

2.2.1 Silicon Vertex Trackers (VTX)

The silicon vertex tracker is working in current PHENIX and two inner pixels layers at radii 2.5 and 5 cm from vertex point and two outer strip-pixels layers at radii 11.8 and 16.7 cm. In case of the sPHENIX, the silicon vertex tracker includes two inner pixels layers and five outer strip-pixels layers in Figure 16. The p_{T} resolution for single pions is shown as a function of p_{T} in Figure 17.

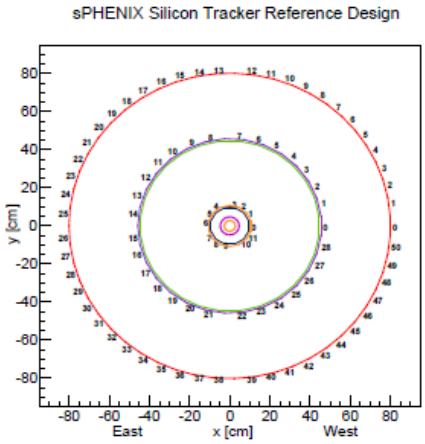

Figure 16: Reconfiguration of the VTX inner two layers and additional tracking layers as explained in the text. [9]

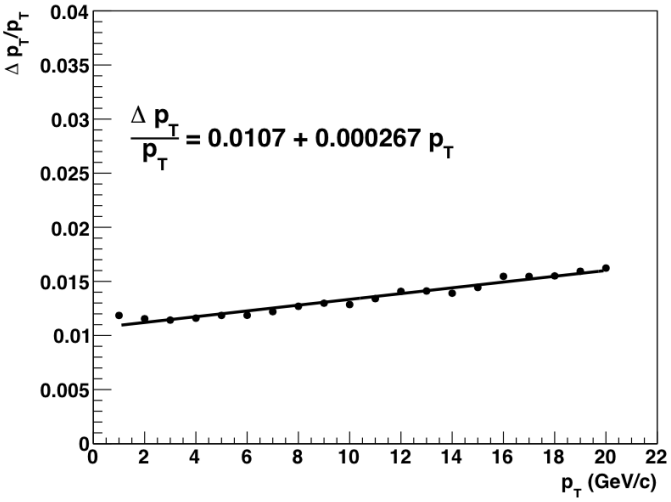

Figure 17: The transverse momentum resolution for single particle (pion). The fit consists of a term that is constant in pT, and a term that is linear in pT. [9]

2.2.2 Electromagnetic Calorimeter (EMCal)

The sPHENIX electromagnetic calorimeter has scintillation fiber in tungsten epoxy as shown in Figure 18, 18 radiation length (X_0) and 12 $\%/\sqrt{E}$ energy resolution as shown in Figure 19 and segmentation of $\delta\eta \times \delta\phi = 0.024 \times 0.024$, and covers a pseudo rapidity range of $|\eta| < 1.1$. It is called SPACAL EMCal.

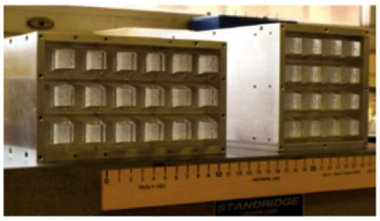

[1]
Prototype built and tested at FNAL (Fermi National Accelerator Laboratory)

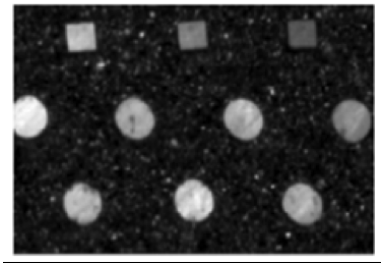

[2]
Scintillation fiber in tungsten epoxy

Figure 18: View of SPACAL Electro-magnetic Calorimeter. [9]

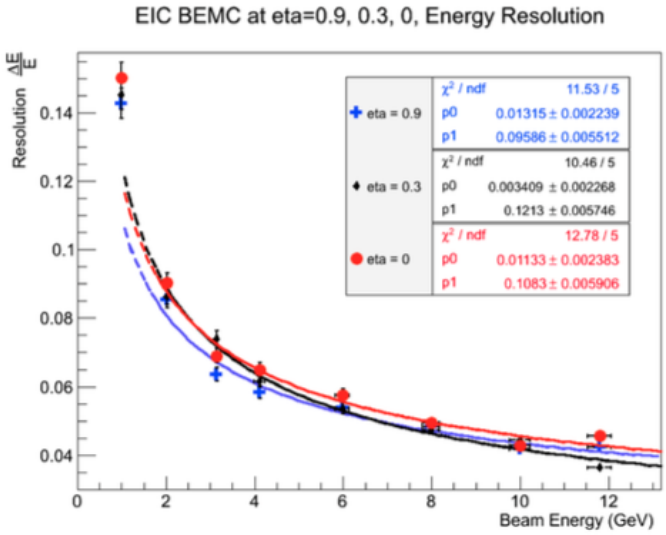

Figure 19: Energy resolution achieved in beam tests of a prototype electromagnetic calorimeter compared with GEANT4 Monte Calro simulation. [9]

2.2.3 Hadron Calorimeter (HCal)

The sPHENIX hadron calorimeter has two longitudinal segments, 5 interaction lengths as shown in Figure34, $100\%/\sqrt{E}$ energy resolution and segmentation of $\delta\eta \times \delta\phi = 0.1 \times 0.1$. Inner HCal is stainless steel and outer HCal is magnet steel.

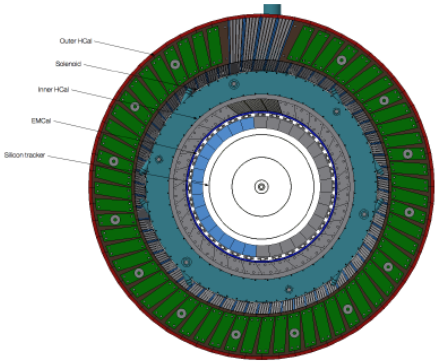

[1] View of sPHENIX barrel

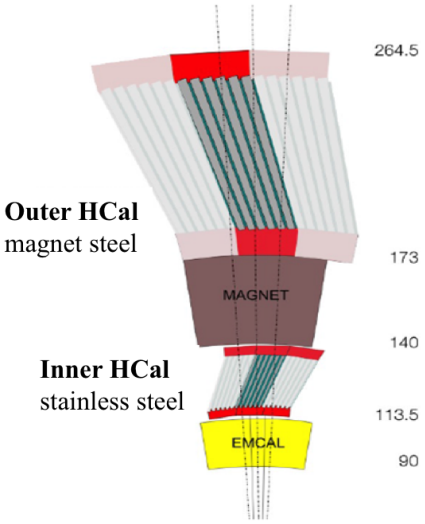

[2] Two longitudinal segments. Inner HCal is stainless and outer HCal is magnet steel.

Figure 20: View of Hadron Calorimeter (HCal). [9]

2.2.4 Pre-Shower (PS)

The Pre-Shower detector is to identify particles and installed in front of the Electromagnetic Calorimeter. Figure 21 shows the concept diagram of the Pre-Shower. The photon identification requires no hit near the surface layer. On the other hands, a charged pion is vetoed by requiring large energy deposited at deep layer. Also separating a single photon from decay two photons requires one hit at deep layer, if the Pre-Shower has good segmentation.

At sPHENIX, the Pre-Shower detector aims at enhancing the physics capabilities of sPHENIX in the following three aspects. Firstly, identification of direct photons in transverse momentum range above 10 GeV/c, where the sPHENIX electromagnetic calorimeter is not capable of discriminating single photons from hadron (mostly π^0) decay, as well as a measurement of direct photons themselves, to a much border kinetic range. Secondly, identification of π^0 via two photon decay channel in the transverse momentum range up to 40 GeV/c. Thirdly, Identification of electron via measurements of upsilon 3 states, where the signal-to-background ratio and the statistics are both critical for a successful measurement. In this thesis, the baseline design of the Pre-Shower is 2.4 X_0 tungsten converter, 0.5 cm$\times$0.5 cm single silicon mini-pad.

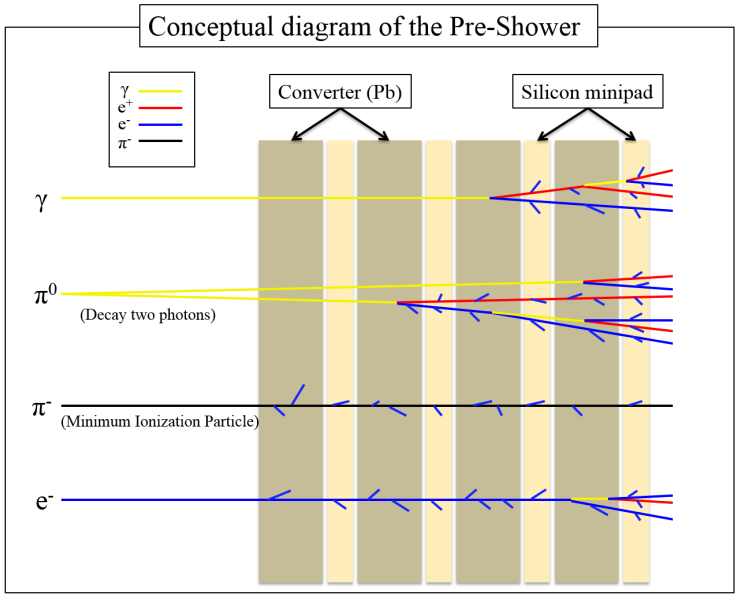

Figure 21: Concept diagram of the Pre-Shower.

3 Analysis Methods

3.1 Simulation and Framework

3.1.1 GEANT4

GEANT4 (GEometry And Tracking) is a computing platform for the simulation of the passage of particles (proton, neutron, electron, and so on) through matter, using Monte Carlo methods. It has many tools of physics process, geometry of detector, visualization, etc. The significance of GEANT4 is expecting a result before experiment. Therefore it is essential for high energy physics, astro physics, nuclear physics.

3.1.2 sPHENIX Frame Work

The sPHENIX simulations has employed the GEANT4 for full detector simulations. It have been integrated with the PHENIX software framework, used analysis tools. The detectors and read out electronics are highly configurable in GEANT4 frame work, making it easy to test various geometries and detector concepts. Magnetic field maps for BaBar magnet have been imported from Opera calculation. We keep every energy deposition and track of each particle, to trace back to the original particle from the event generator.

3.2 Energy Calibration

3.2.1 Energy Resolution

The energy resolution is calculated by the energy spectrum which is obtained by the GEANT4 simulation. It is expressed in the following formula.

$$\frac{\sigma}{E} = \frac{p_0}{\sqrt{E}} + p_1 \tag{5}$$

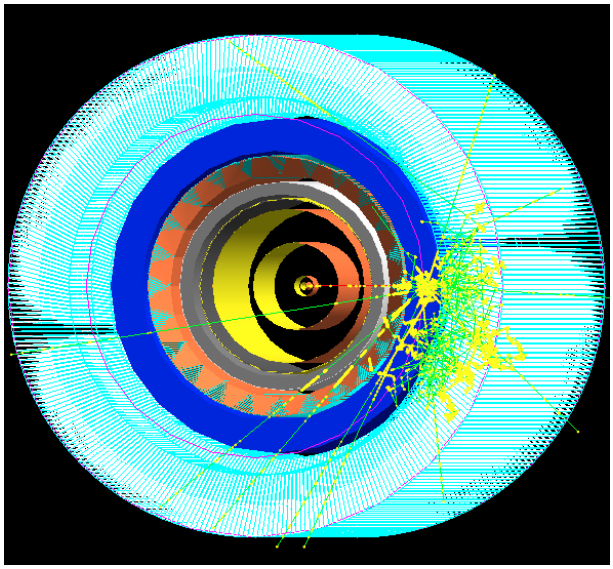

Figure 22: GEANT4 simulation at sPHENIX

At the left side of a formula, σ is a variance of distribution and E is a measured energy. The right side of a formula show a fitting function as a function of the measured energy. Where p_0 and p_1 are the fitting parameters. At low momentum region, the p_0 is dominant and determines the resolution curve. On the other hands, the p_1 is dominant at high momentum region. Figure 23 shows the energy distributions measured by the Pre-Swoer and the EMCal. It is fitted by the Gauss function.

3.2.2 Sampling Fraction

A sampling fraction is inverse of a calibration constant and used to reconstruct energy. It is expressed in the following:

$$\text{SamplingFraction} \quad = \quad \frac{E_{\text{vis}}}{E_{\text{invis}} + E_{\text{vis}}} \tag{6}$$

Where E_{vis} is a deposited energy in the detector, E_{invis} is the deposited energy in the converter. In other words, a sampling fraction is a ratio of the detectable energy to total deposited energy in the detector. The sampling fraction of detectors depends on ratio of amount of substance between a converter and a detector, and is related with the energy resolution. At the sPHENIX, sampling fraction of the EMCal is 2.6 %. So we should optimize the design of the Pre-Shower with little effect on EMCal resolution. Table1 shows sampling fractions each radiationn length (X_0) of the Pre-Shower.

Where the silicon is same thickness of 0.006 cm. As shown in table, if the converter thickness of the Pre-Shower is less than $1.6X_0$, its sampling fraction is less than the EMCal. However the identification of electrons and photons need enough amount of substance, because probability of electromagnetic shower caused depend on it. So we should have several candidates of the Pre-Shower which are $1.6X_0$, $2.0X_0$ and $2.4X_0$.

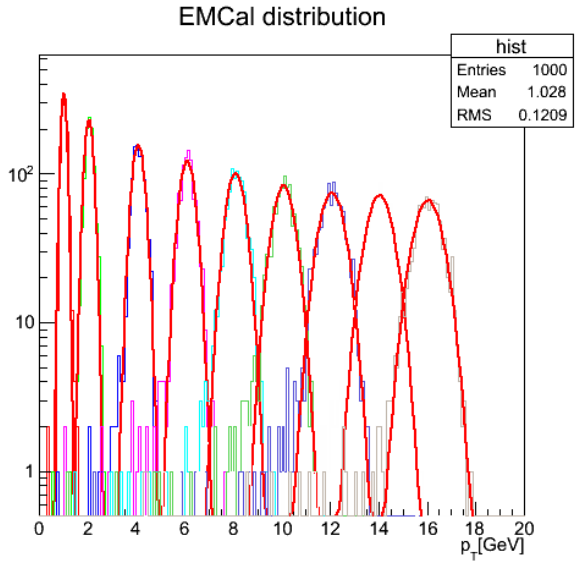

Figure 23: The energy spectrum with GEANT4 and single particle simulation. It is fitted by the gauss function.

3.3 Detected Procedures

3.3.1 Single Photon Identification

Main motivation of the Pre-Shower detector is to separate direct photon from decay photons from high transverse momentum π^0. Opening angle of decay 2 photons from high transverse momentum π^0 is very narrow. Therefore their causing electromagnetic showers are merged and they are identified as single photon at the EMCal. So an early developing electromagnetic shower should be measured using very thin and good segmentation Pre-Shower detector. In this thesis, the methods of single photon identification are in the following.

1, Number of hits.

In case of ideal condition, single photon hit one cell in the Pre-Shower. On the other hands, π^0 decay 2 photons hit two cells as the Figure 24. So identification of direct photon requires one hit on the Pre-Shower with the appropriate threshold and the region cut which is the size of the EMCal cluster. Figure 25 shows the number of hit cells with 10MeV threshold in case of single photons and single π^0. As shown in figure, the direct photon identification becomes possible by requiring only one hit. Also a case of no hits at the Pre-Shower is identified as a single photon.

2, Ratio of the max cell energy to the sum cells energy.

In case of single photon, the ratio of the highest cell energy to the sum cells energy should be almost one, because the electromagnetic shower from the single photon goes in one cell. On the other hands, ratio of π^0 decay photons should be about 50%, because two photons occur electromagnetic shower. As shown in figure 26, the distribution is different between single photon and π^0 and the peak at one shows only one hit at the Pre-Shower.

3, Shower Shape.

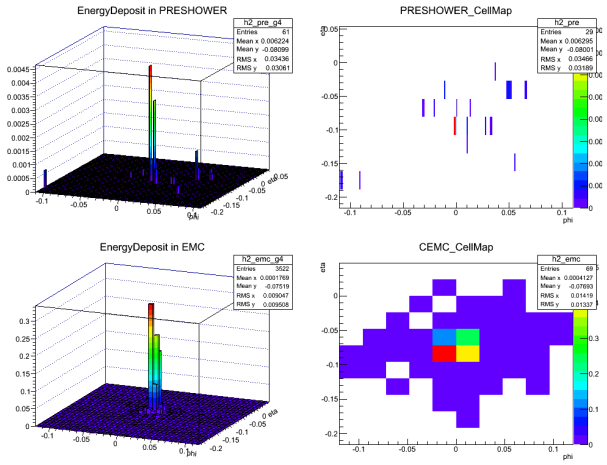

Figure 24: Event display for decay two photons from π^0 at the Pre-Shower and the SPACAL

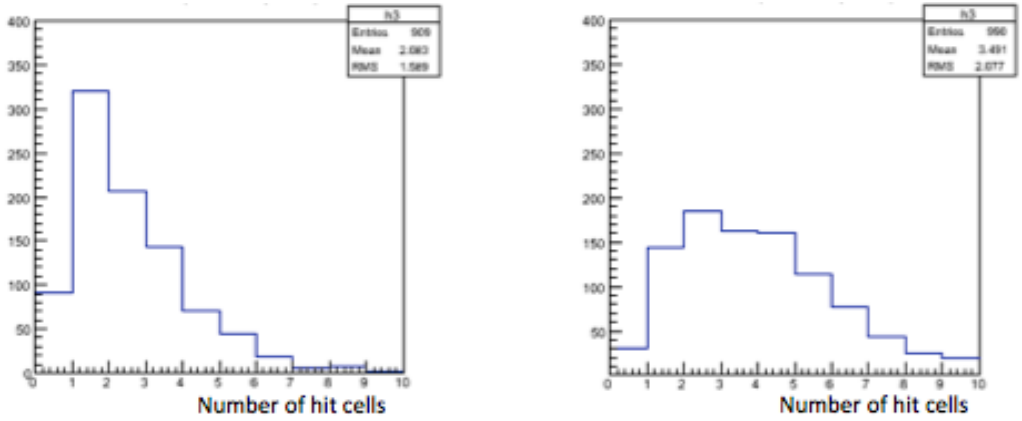

[1] single photon [2] single π^0

Figure 25: Number of hit cells with 10MeV threshold

Table 1: Sampling Fraction

Tungsten Radiation Length	Matter	Mean Energy	Stat. Err.	Sampling Fraction
$2.4X_0$	Tungsten	57.5 MeV	32.3 MeV	1.9%
	Sillicon	1.1 MeV	0.8 MeV	
$2.0X_0$	Tungsten	37.1 MeV	21.8 MeV	2.3%
	Sillicon	0.9 MeV	0.7 MeV	
$1.8X_0$	Tungsten	29.0 MeV	17.4 MeV	2.5%
	Sillicon	0.7 MeV	0.6 MeV	
$1.6X_0$	Tungsten	22.3 MeV	13.7 MeV	2.7%
	Sillicon	0.6 MeV	0.5 MeV	
$1.2X_0$	Tungsten	12.4 MeV	7.6 MeV	3.3%
	Sillicon	0.4 MeV	0.4 MeV	
$1.0X_0$	Tungsten	8.8 MeV	5.3 MeV	3.7%
	Sillicon	0.3 MeV	0.3 MeV	
$0.6X_0$	Tungsten	3.9 MeV	2.1 MeV	5.1%
	Sillicon	0.2 MeV	0.2 MeV	

In case of developing EM shower, hit distribution of π^0 decay photons is formed as ellipse. So its covariant matrix of ϕ and η become larger than that in the case of single photon. Shower shape is defined as following equation.

$$\sigma^2_{\phi,\eta} = \frac{\Sigma_i w_i(\phi_i - \bar{\phi})(\eta_i - \bar{\eta})}{\Sigma_i w_i} \tag{7}$$

where ϕ_i and η_i are position of the each cell, $\bar{\phi}$ and $\bar{\eta}$ are the center of the energy cluster, w_i is the weight parameter described as follow:

$$w_{\mathrm{i}} = \max(0, \mathrm{w_0} + \ln\frac{\mathrm{E_i}}{\mathrm{E}}) \tag{8}$$

where E_{i} is energy in each cell, E is the sum energy in the cluster, w_0 is called the free weight parameter is determined by position resolution. Figure 27 shows the position resolution of the Pre-Shower as a function of w_0. As a result, the position resolution is the best at w_0 of 6.0.

Figure 28 shows the distribution of shower shape for each particle and threshold. The blue histogram shows a single photon, and the red histogram shows a single π^0 for each threshold. As shown from these results, there are almost no difference in the shower shape. So the shower shape is not useful for the direct photon identification.

3.3.2 Multi-layers Pre-Shower

We should study the multi-layers Pre-Shower for good separation of direct photon from decay photons. It was assumed total radiation length of 2.4 X_0 included 10 layers (i.e. (0.24 X_0 + silicon detector) $\times$ 10). Figure 31 shows the number of hits in each layer at p_T

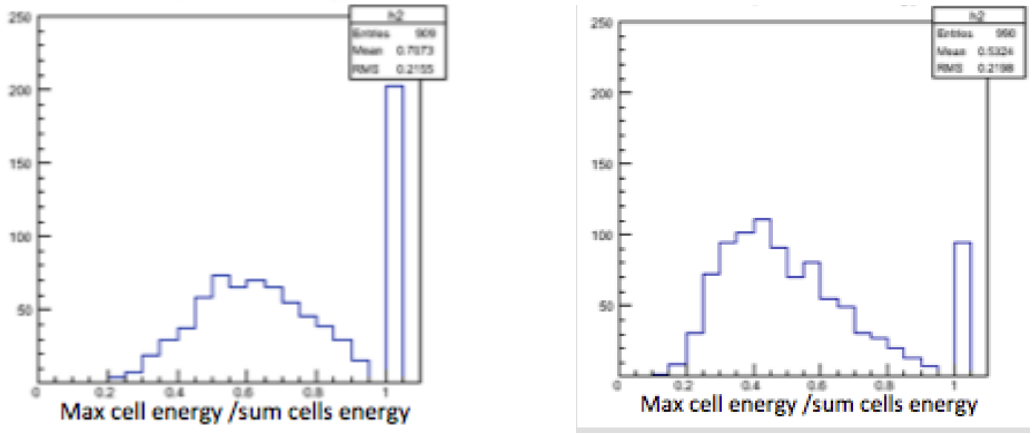

[1] single photon [2] single π^0

Figure 26: Ratio of max cell energy to sum cells energy with 10MeV threshold

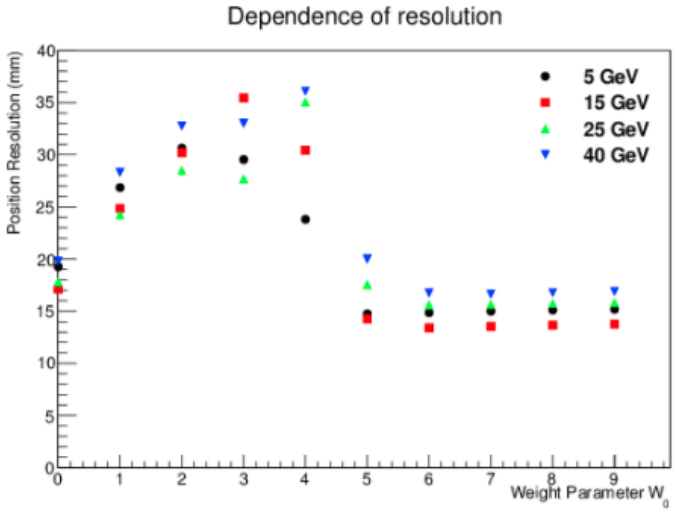

Figure 27: Position resolution as a function of weight parameter w_0

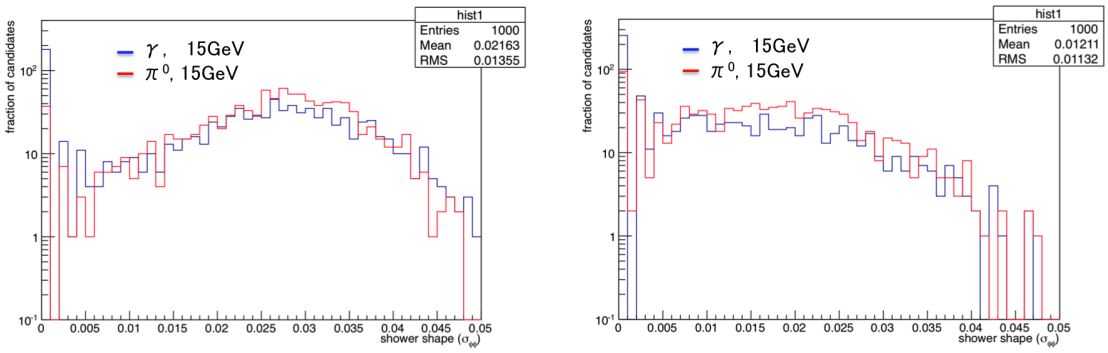

[1] 0MeV threshold [2] 10MeV thereshold

Figure 28: Shower shape at the Pre-Shower

= 15 GeV. The red histograms show a single photon at 15 GeV and the blue histograms show a single π^0 at 15 GeV. The difference in distributions at hits = 0 become conspicuous with each layer of depth, because the probability of electron pair creation vary from the number of photons. So we should require no hit on layer of the Pre-Shower for identifying a single photon.

Figure 30 show the sum energy deposited in each layer. The red histograms show a single photon and the blue histograms show a single π^0 and the green histograms show a single π^- of $p_T = 15$ GeV. The difference in distributions between the single photon and the single π^0 become conspicuous with each layer of depth as the number of hits. On the other hands, the distribution of the single π^- are same, because these are minimum-ionization particles. In other words, almost all of single π^- deposit energy at the silicon detector with the ionization loss. So separating a single photon from charged hadron requires no energy deposit near the surface, or large energy deposit at deep areas of the Pre-Shower. However charged hadrons are vetoed with the tracking and the ratio of momentum to energy at the sPHENIX. So the design of the Pre-Shower is based on to separate photons from decay photons. If we read out double layers, we should select deep areas of the Pre-Shower. In this thesis, the design of double layers Pre-Shower is to read out 7 and 10 layers. Figure 31 show the correlation of the number of hits at 7 and 10 layers. The left plot shows the single photons and the right plot shows the single π^0. As show from this, the single π^0 are vetoed by requiring hits = 0 in each layer.

3.3.3 Electron Identification

In this section, the identification (ID) of electrons is described. Leptons are the primary signature of electro-weak processes. They are used in a lot of physics analysis. Electron ID, separating electrons from charged hadrons background. Electrons are identified by ratio of momentum to deposited energy, hit cells and shower shape. At the electromagnetic calorimeter, electrons can deposit large energy, hit many cells with developing electromagnetic shower. On the other hands, charged hadrons can hardly cause electromagnetic shower, because its mass is very much lager than electron mass (i.e these are minimum ionization particles).

Figure 32 show difference of developing shower between electrons and charged pions.

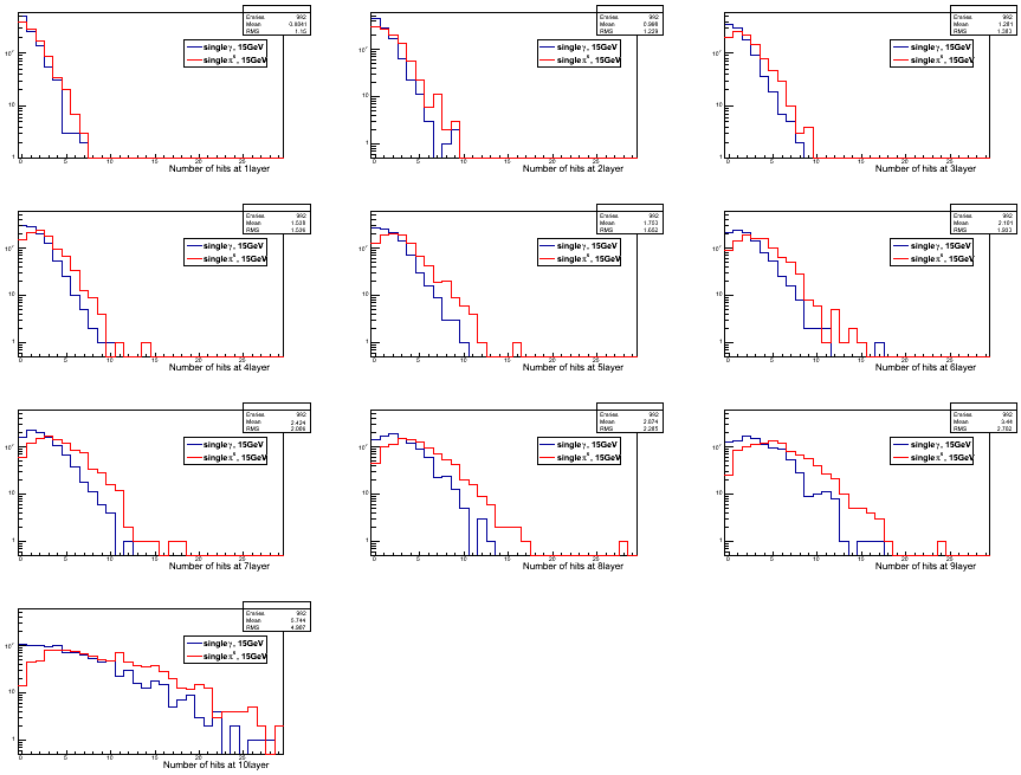

Figure 29: Number of hits each layers

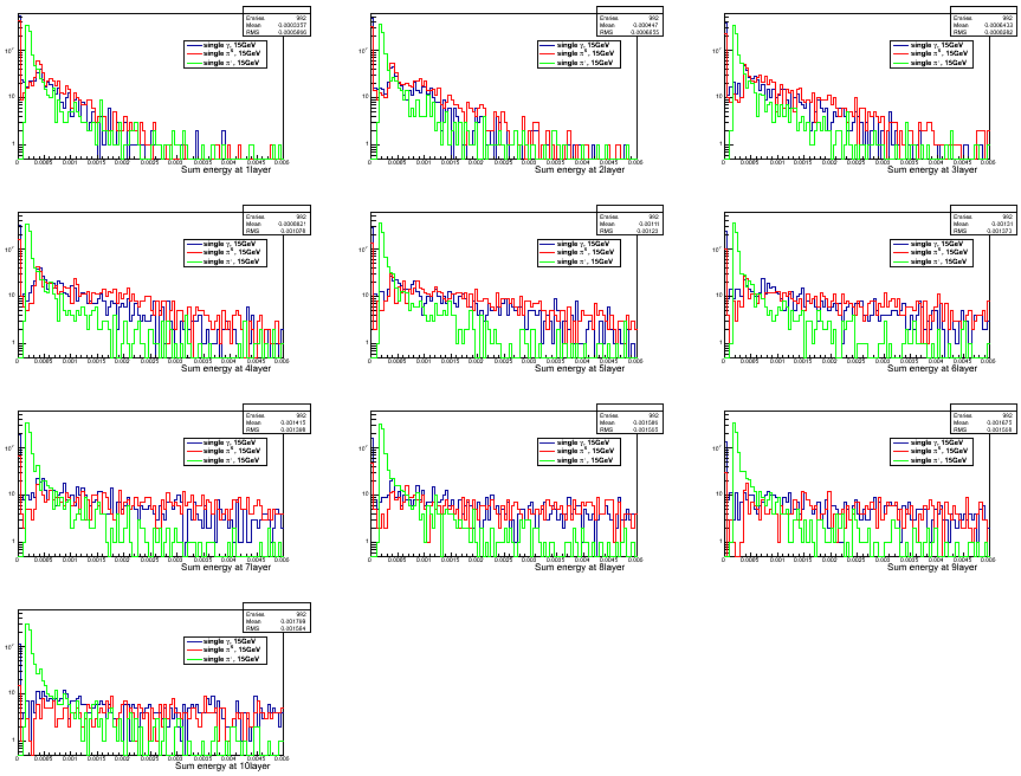

Figure 30: Sum energy in each layer

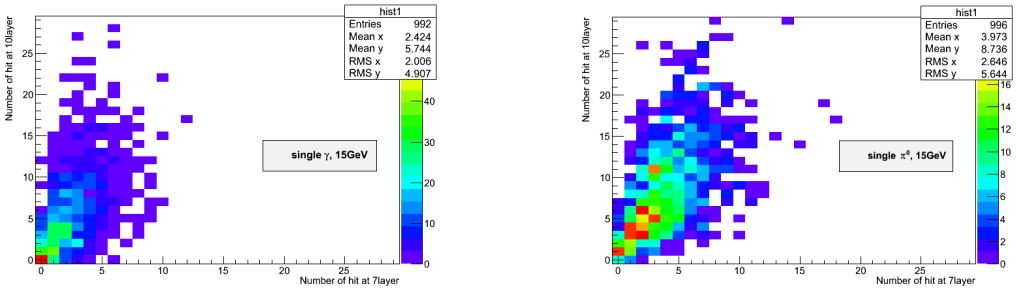

Figure 31: Correlations of hits between at 7 layer and at 10 layer

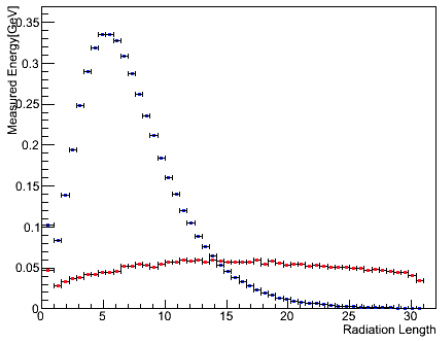

[1] Deposited energy as a function of radiation length

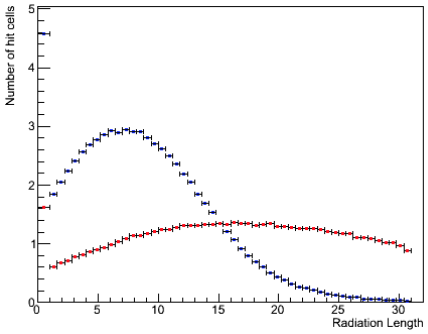

[2] Number of hits as a function of radiation length

Figure 32: Electromagnetic shower development

It plots energy deposit in each layer as a function of radiation length with the single particle simulation using the GEANT4. In this simulation, the total radiation length is $31X_0$, including the Pre-Shower of 1 layer ($1X_0$), and the sampling electromagnetic calorimeter of 50 layers ($0.6X_0 \times 50$). The first point shows energy deposit or hit cells in the Pre-Shower, other points show energy deposit or hit cells in each layer in the sampling electromagnetic calorimeter. As shown in figure 32, the identification of electrons become possible with difference of developing shower. But practically we cannot read out all layers of sampling calorimeter in cost. So we should read out three places that are the Pre-Shower, the EMCal and the HCal.

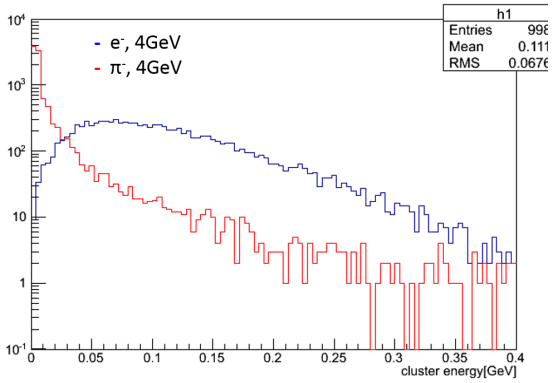

[1] preshower

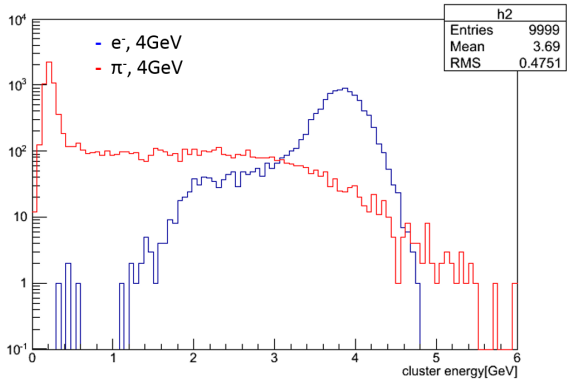

[2] EMCal

Figure 33: Measured energy distribution

Figure 33 shows the distribution of cluster energy at the Pre-Shower and the EMCal. As shown in Figure 33 on the left plot, many charged pions hardly deposit energy in the Pre-Shower. On the other hands, electrons deposit large energy. Also some charged pions deposit large energy because of causing hadronic interactions. At the EMCal, electrons deposit almost all energy. Thus the distribution of cluster energy deposited by electrons become a gaussian distribution. The cause of tail at low energy is due to magnetic field

by BaBar magnet, that is say, the electromagnetic shower is deformed. On the other hands, the distribution of charged hadrons have two components. The peak at 0.3 GeV is produced by minimum ionization particles. Another component is produced by hadronic interactions.

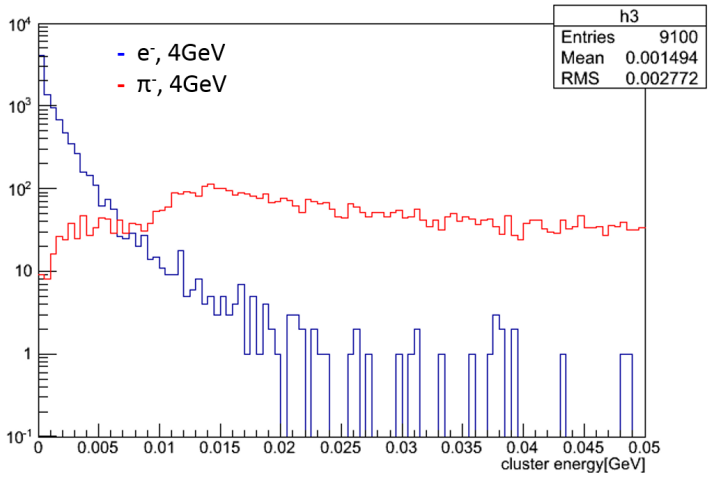

Figure 34: HCal scintillator energy

Figure 34 shows the distribution of the energy deposited at scintillator of HCal. As shown in the figure, electrons hardly deposit energy in the HCal, because these deposit almost all energy in the EMCal. On the other hands, Almost all charged pions deposited large energy by hadronic interactions. As shown from these results, we can separate electrons from charged hadrons by the energy cut for each calorimeter.

4 Results and Discussions

In this thesis, 2 topics of the Pre-Shower detector and particle identification are discussed.

4.1 Design and Performance Study for the Pre-Shower Detector

At the beginning of this section, the design of the Pre-Shower is decided by Monte Calro and GEANT4 simulations. Next the occupancy and energy resolution were evaluated in case of that design. Furthermore the method of separating direct photon from π^0 decay photons is described, and the fraction of direct photon identification to π^0 decay photons miss identification is evaluated.

4.1.1 Design Optimization of the Pre-Shower

I and Ueda made the simulator including generator of π^0 and decay process based on the Monte Calro simulation for deciding segmentation of the Pre-Shower. Figure 35 shows the minimum opening angle of decay 2 photons from π^0 as a function of the transverse momentum. At least the Pre-Shower segmentation should be less than 0.01 rad for identifying decay 2 photons from 40 GeV/c π^0. Figure 36 shows the distribution of the opening angle at p_T 40 GeV/c. The opening angle becomes minimum in case of decaying vertically to direction of π^0 on rest frame of π^0. The right plot shows the correlation between ϕ and η of opening angle.

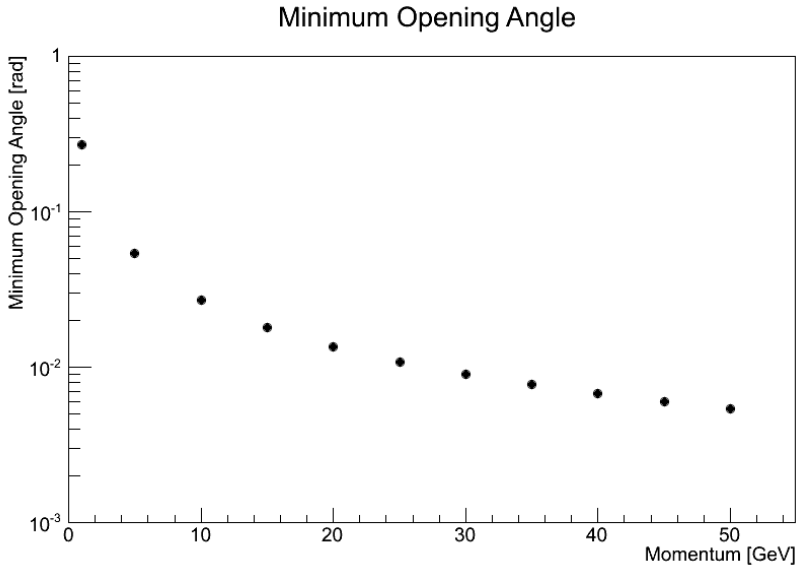

Figure 35: Minimum opening angle of decay photons from π^0 as a function of the transverse momentum.

Figure 37 shows detection efficiency of 40 GeV π^0 as a function of shape of cell under condition of constant area, that is to say, $d\phi \times d\eta = 0.01$. This simulation assumed the perfect Pre-Shower detector, i.e, it is evaluated by only geometry. In the case of square or thin rectangular, detection efficiency is high.

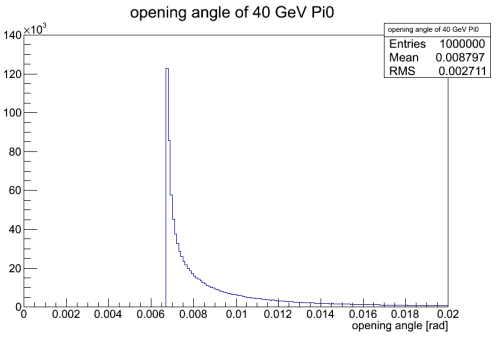

[1] Opening angle of decay photons from π^0.

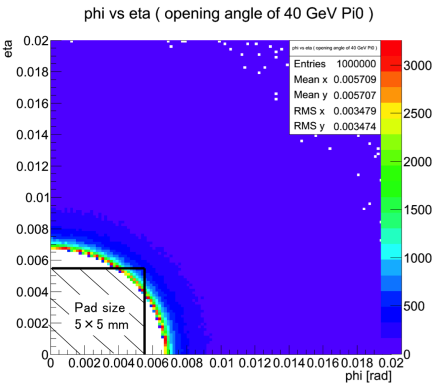

[2] Correlation of ϕ and η.

Figure 36: Opening angle of π^0 at $p_T = 40$ GeV

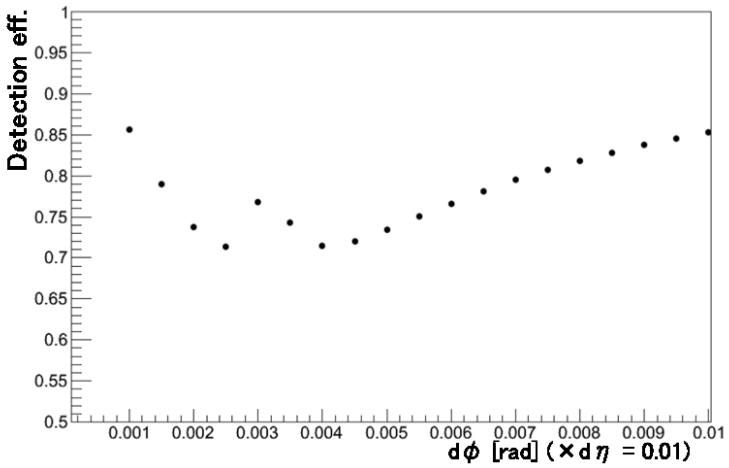

Figure 37: Detection efficiency for perfect Pre-Shower as a function of dϕ under condition of constant area of cells.

Figure 38 shows the detection efficiency of π^0 for each size of cell and p_T. The detection of π^0 is defined as that cells hit by π^0 decay photons are separated by two cells or more. The red and the blue closed circles show shape of square, and the red and the blue filled opened circle show shape of oblong. At $p_T \leq 35$ GeV, the segmentation of 5×5 mm is the best detection efficiency. Also the Pre-Shower segmentation should be less than EMCal segmentation (24×24 mm), because the position resolution of the Pre-Shower should be lower than the EMCal. In light of these, the segmentation of 5×5 mm is good. So its segmentation was defined as a base design.

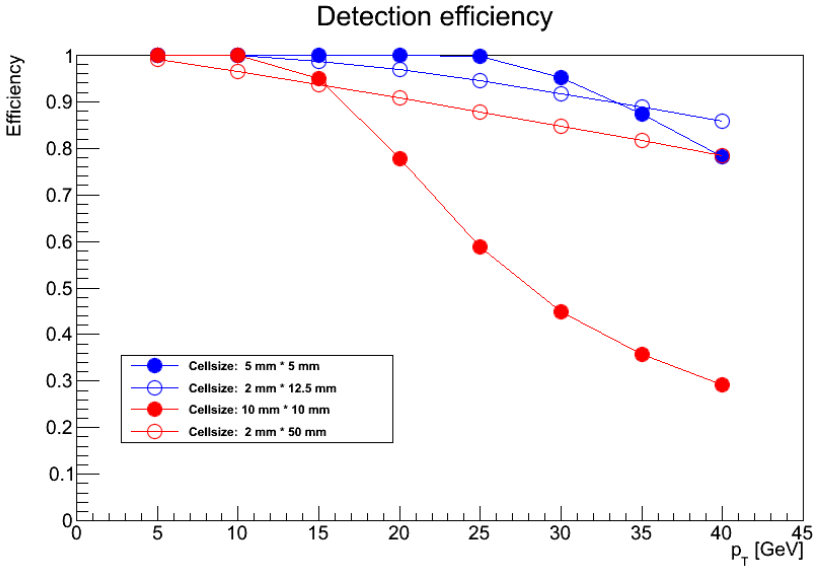

Figure 38: Detection efficiency as a function of transverse momentum in case of perfect Pre-Shower

4.1.2 Energy Resolution

The Pre-Shower detector will be installed in front of the electromagnetic calorimeter. So the effect on the EMCal energy resolution should be evaluated in the case with and without the Pre-Shower. Also the energy resolution depends on thickness of convertor. Figure 39 shows the energy resolution as a function of transverse momentum, evaluated by simulation of single electrons and the GEANT4 simulation. The blue points show the case with PS ($2.4X_0$) and the green show the case with PS ($1.6X_0$) and the read show the case without PS. The difference of resolution between with and without the Pre-Shower is less than 1 %. As a result, there is little effect of the additional detector on the energy resolution of sPHENIX for electromagnetic particles.

4.1.3 Occupancy

In case of high energy nucleon collisions, occupancy needs to be evaluated firstly. Because the number of hit cells affect strongly identification of single particle under condition of high multiplicity. The occupancy of the Pre-Shower was calculated using HIJING (event generator for heavy ion collision) and GEANT4 simulation. There were 894 hit cells out of

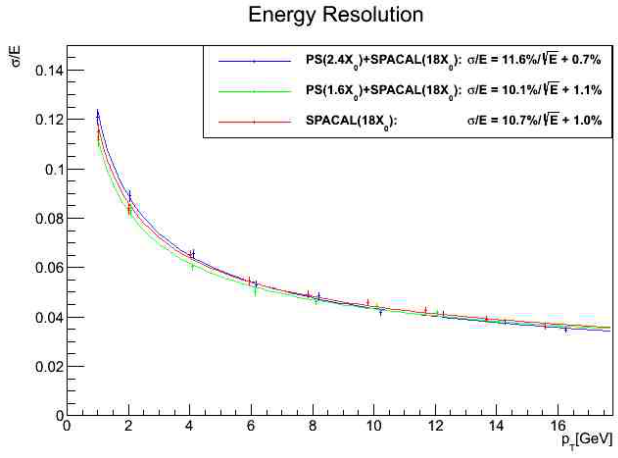

Figure 39: Energy resolution as a function of transverse momentum.

35k in average of 100 events. And the average number of cells in clusters was factor of 1.3. $dN_{ch}/d\eta$ was 614 in range of $\eta = \pm$ 0.275. As a result, the occupancy of the Pre-Shower was 2.5 % in HIJING Au + Au at b = 0 fm and it can be accepted.

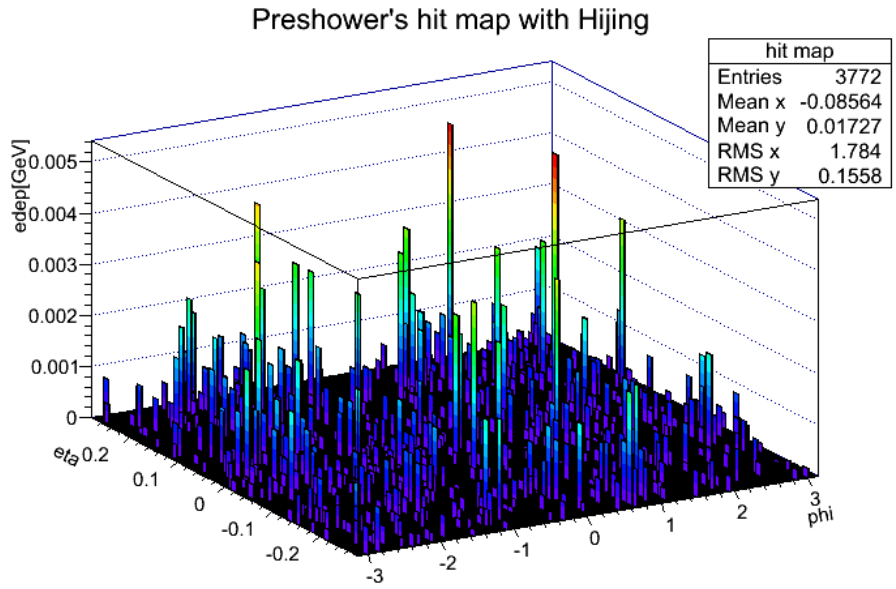

Figure 40: Event display for HIJING most central Au+Au collisions

4.2 Particle Identification at sPHENIX

In this section, the results of performance of particle identification at sPHENIX are shown. Firstly, the photon identification fraction is evaluated. It is the fraction of identification of photon and misidentification of decay photons. The enhancement factor is evaluated

by using these results. Secondly, the efficiency of identification of electrons and charged pions are evaluated with full GEANT4 simulation. The pion rejection is evaluated by using these results.

4.2.1 Photon Identification Fraction

Figure 41 show the photon identification fraction which is the probability of identifying a single photon or mis-identifying a single π^0 as a single photon. The blue points show fraction using the EMCal, the red filled and open points show the fraction using the Pre-Shower. In case of using the EMCal, a single photon is identified by that a reconstructed mass of π^0 is out of 3 sigma from its mean. As a result, the EMCal can not separate a single photon from a single π^0 above 5 GeV in p_T, because two electromagnetic shower from π^0 are merged. On the other hands, the Pre-Shower can separate a single photon from a single π^0 at wider transverse momentum. At next section, the ratio of identification of a single photon to misidentification of a single π^0 will be discussed.

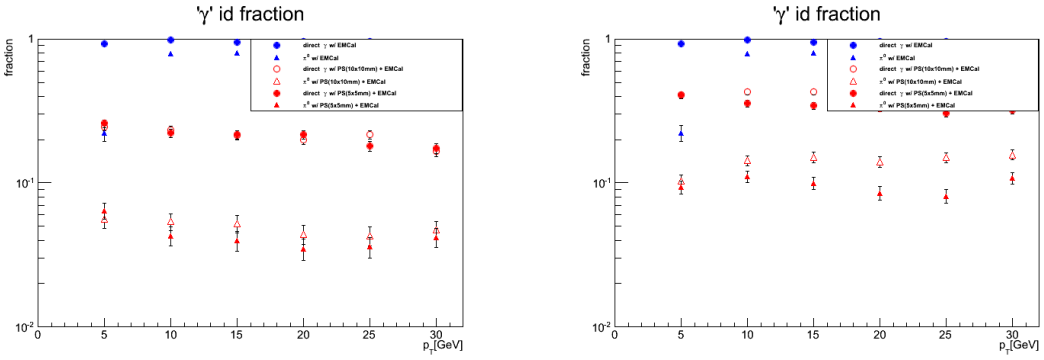

[1] No thereshold [2] 10 MeV threshold

Figure 41: Photon ID fraction

Table 2: Cut variables for identifying a single photon

Variables	Required cuts
Number of hit cells with Pre-Shower	$N_{hit} \leq 1$
Ratio of max deposited energy to sum energy	$0.8 \leq E_{max}/E_{sum}$

4.2.2 Enhancement Factor for Direct Photon

Figure 42 show enhancement factor of signal-to-background ratio of direct photon for each threshold as a function of transverse momentum. The red points show case of using the Pre-Shower of 5×5 mm segmentations and 10×10 mm segmentations, and the blue points show case of using the EMCal. At the good case (i.e. no threshold), the enhancement factor for the case the Pre-Shower is in the range from 4 to 7 at 5 GeV $\leq p_t \leq$ 40 GeV. On the other hand, the enhancement factor for the case the EMCal are around 1.0 at 10 GeV $\leq p_t \leq$ 40 GeV. As shown from this result, the signal-to-noise ratio of direct photon

is enhanced by a factor from 4 to 6 by using the Pre-Shower. Also in case of the bad case (i.e. 10 MeV threshold), its factor are from 3 to 4.

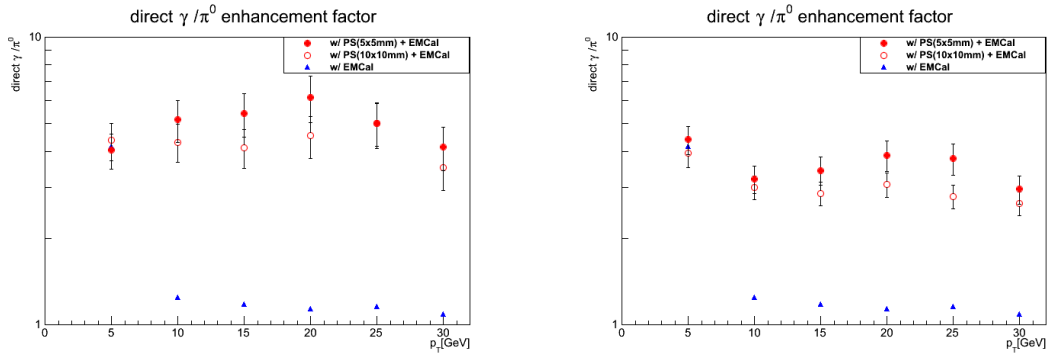

[1] 10MeV threshold [2] Zero threshold

Figure 42: Enhancement Factor of a single photon to a single π^0

4.2.3 Multi-layers Pre-Shower

The design of the multi-layers Pre-Shower was studied for improvement of the direct photon purity. In this simulation, the multi-layers Pre-Shower has ten layers. The layer 7 and layer 10 are read out for evaluating the two layers Pre-Shower. The left plot in Figure 43 shows the enhancement factors as a function of transverse momentum. The red points show enhancement factor for no hit on both layer 7 and layer 10 at Pre-Shower and the blue points show the enhancement factor for no hit on layer 10 at Pre-Shower. In case of no hit. the enhancement factors of using both layers are less than that of using layer 10. Therefore, the enhancement factor do not improve by reading out multi layers in the case requiring no hit is in each layer.

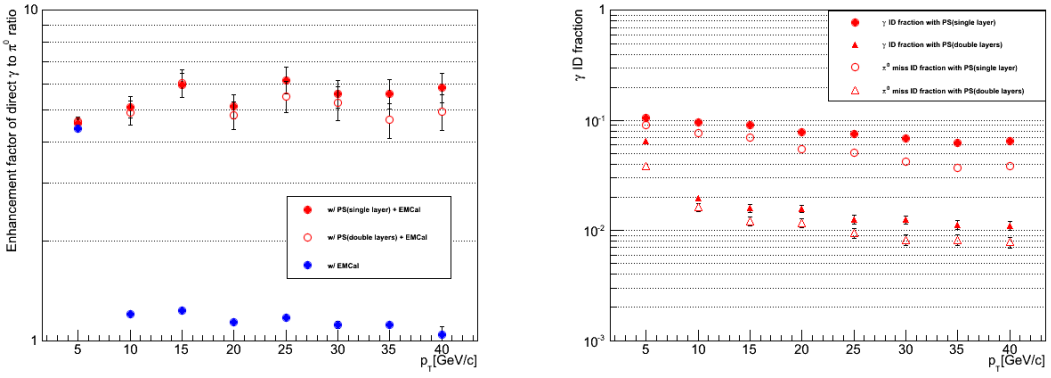

Figure 43: Enhancement factor for Multi-layer design

4.2.4 Electron Identification

For electron identification, some variables were measured and calculated from the Pre-Shower, the EMCal and the HCal. In this section, the electron identification is described using each calorimeter. First of all, the case of using the Pre-Shower and the EMCal is discussed. Figure 44 show the correlation of energy measured by the Pre-Shower and the EMCal. The right figure shows correlation after applying cut. The required cut values for electron ID are in the following table. As a result, the pion rejection was the factor of 1160 at 70 % electron efficiency by applying these cuts. Also in case of using only the EMCal, it is the factor of 166 at 70 % electron efficiency. That is say, the pion rejection is improved by one order of magnitude by using the Pre-Shower. Secondly, the electron ID with the inner HCal is discussed. The left histogram on the Figure 45 shows the leaked energy from the EMCal in the inner HCal, and the right histogram show the leaked energy after electron identification with the Pre-Shower and the EMCal. As shown in figure, the leaked energy in the inner HCal is good tool for the electron ID. The pion rejection is about 100 at 90 % electron efficiency with only inner HCal. Incidentally, the measurement of upsilon meson requires 100 pion rejection at 90 % electron efficiency. So the pion rejection with 3 calorimeters is discussed in the next section.

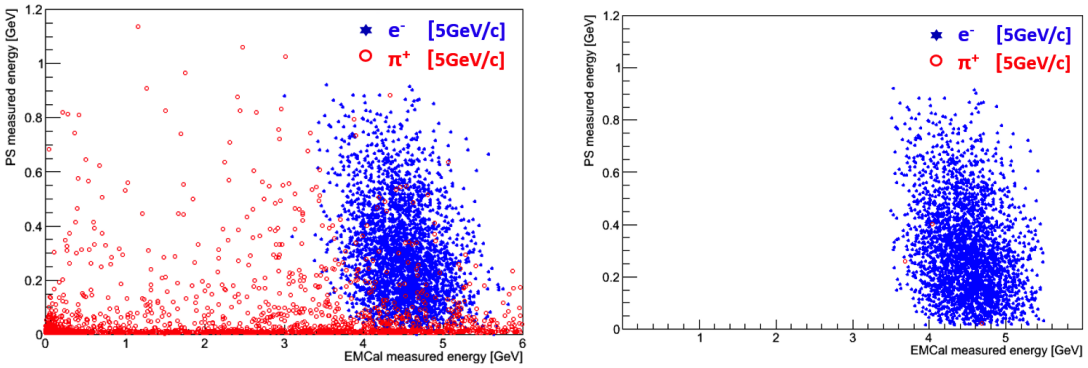

[1] Before applying cut

[2] After applying cut

Figure 44: Energy correlation between Pre-Shower and EMCal

Table 3: Cut variables for identifying a electron

Variables	Required cuts
Energy measured with Pre-Shower	0.002 GeV $\leq$ E $\geq$ 0.026 GeV
Energy momentum matching	$3.8/5 \leq E/p_T \geq 5.4/5$
Number of hit cells with Pre-Shower	$2 \leq N_{hit}$
Number of hit cells with EMCal	$8 \leq N_{hit} \geq 20$
Difference of mean position	$0.004 \leq \sigma_\phi \leq 0.01$

4.2.5 Pion Rejection

In this section, the total pion rejection with the sPHENIX calorimeters are discussed. Figure 46 show the pion rejection in each calorimeter as a function of the electron efficiency.

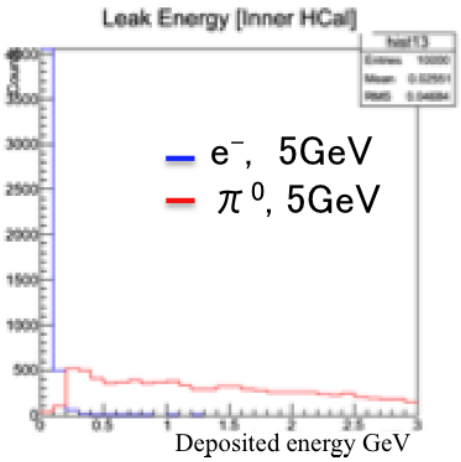

[1] Leaked energy distribution

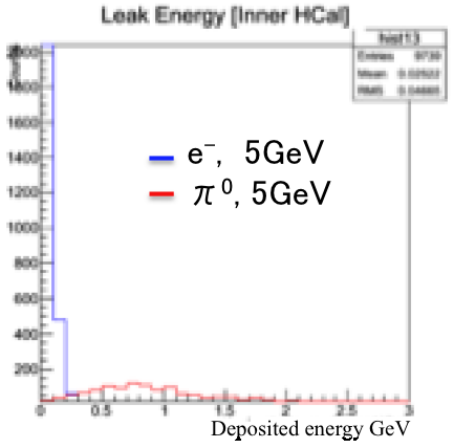

[2] Leaked energy distribution after applying cut with the Pre-Shower and the EMCal

Figure 45: Leaked energy distribution

In this figures, only the cut of measured energy in each calorimeter is used. As shown in this figure, the pion rejection with the HCal was the most highest in calorimeters at 90 % electron efficiency. So the total pion rejection should be evaluated, based on the cut variables of the inner HCal. That is say that the cut variables of the inner HCal is changed from 100 % to 80 %, and the cut variables of the Pre-Shower and the EMCal are constant which are 98 % efficiency at the Pre-Shower and 99 % efficiency at the EMCal. Figure 47 shows the total pion rejection as a function of the electron efficiency with tree calorimeters. The red points are with three calorimeters, and the blue points with the EMCal and the inner HCal. As shown from the Figure 47, the total pion rejection was improved by a factor of two using the Pre-Shower. In case of using three calorimeters, the total pion rejection is 200 at 90 % electron efficiency. It is sufficient for the upsilon measurements.

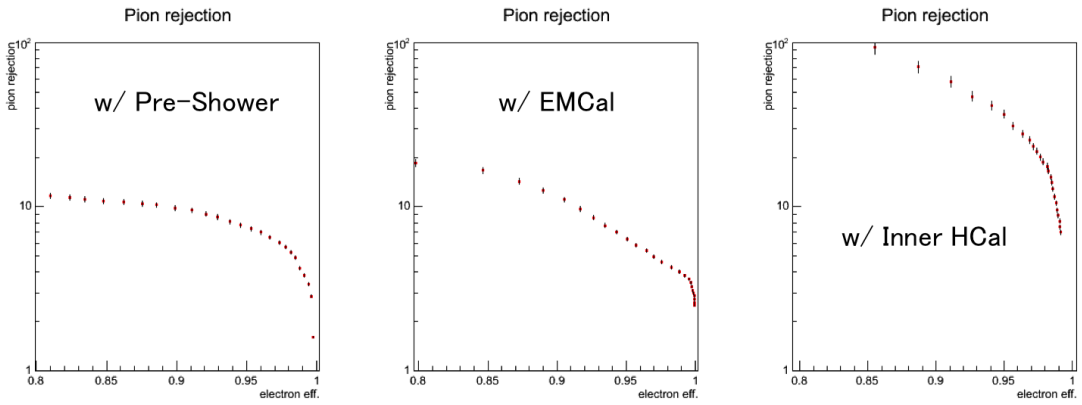

Figure 46: Pion rejection in each calorimeter as a function of electron efficiency

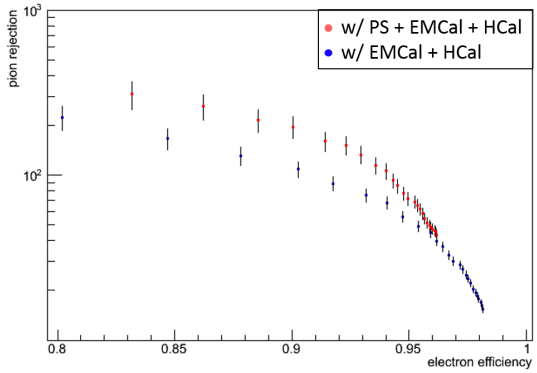

Figure 47: Total pion rejection as a function of electron efficiency

5 Summary and Conclusions

We have studied the design of the Pre-Shower detector and the particle identification at sPHENIX. Firstly, we have decided the design of Pre-Shower detector that is the segmentation of 5×5 mm, the converter radiation length of 2.4 X_0. In this conditions, the enhancement factor of direct photons to decay photons from π^0 ratio is 6, that is to say, the signal-to-noise ratio becames 10 times at p_T range from 5.0 GeV to 40 GeV in the Figure 48. Especially, it is over 3 at above p_T of 15 GeV. These results show the measurement of direct photons is enabled. Furthermore, we have evaluated the design of multi-layers Pre-Shower for improving the direct photon to π^0 ratio. However the enhancement factor did not improv in case of reading out 2 layers Pre-Shower. This is considered that the direct photon to π^0 ratio depend on converter thickness but not number of read out. So we should thicken converter of the Pre-Shower, if we want to further improve it.

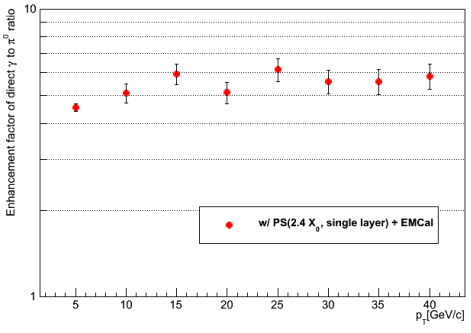

[1] Enhancement factor of direct photon to decay photons ratio

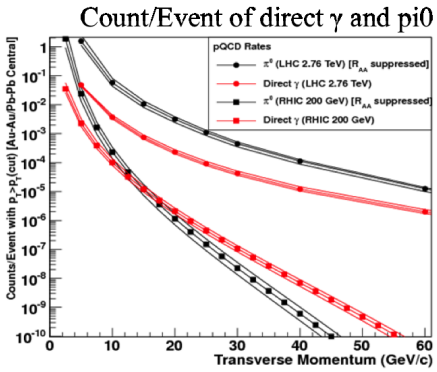

[2] Count per event of direct photon and π^0 [9]

Figure 48: Signal-to-noise ratio for direct photon measurement

Secondly, we have established the method of the electron identification at sPHENIX. The total pion rejection is 200 at 90 % electron efficiency by using 3 calorimeters in the

left plot on Figure 49. The right plot show the upsilon mass spectrum in case of pion rejection = 90 and electron efficiency = 90 %. In this condition, the signal-to-noise ratio of the upsilon measurement is above the unity. As a result, the measurement of upsilon meson with three states is measurable.

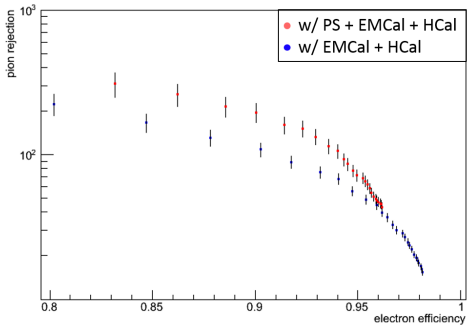

[1] Total pion rejection as a function of a electron efficiency

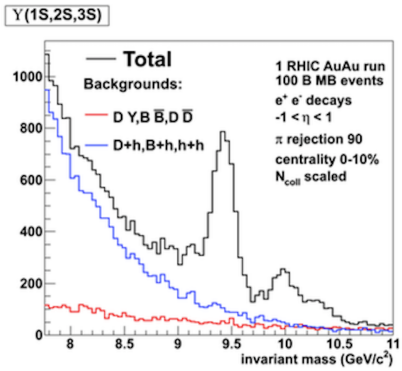

[2] Upsilon mass spectrum for ten billion 0-10 % central Au+Au events [9]

Figure 49: Pion rejection for the measurement of upsilon meson

In this thesis, the enhancement factor of direct photons to decay photons, and the total pion rejection are evaluated by using a single particle simulation, but practically these shouldd be evaluated under condition of high multiplicity in heavy ion collisions. Therefore it is challenges for the future.

6 Acknowledgements

I would like to thank my supervisor Prof. K.Shigaki. He gave me the thesis topics and valuable advises. I could not have done this work without his support. I would like to greatly appreciate Assistant Prof. K.Homma for his guidance and encouragement in PHENIX BBC subsystem group. Not only so, but he showed a good example as scientist. I would like to express my gratitude to Dr. Y.Akiba for his valuable advises. Not only so, but he gave me the next topic and interest of heavy ion collisions experiment. I am grateful to Prof. T.Sugitate and Assistant Prof. T.Miyoshi for their useful comments.
I would like to express my appreciation to whom I worked together in the Hiroshima group. Dr. Y. Nakamiya, Mr. S. Yano, Mr. T. Hoshino, Mr. T. Hasebe and Mr. T. Okubo taught me detail of analysis methods and PHENIX BBC work. I had an enjoyable thesis work with Mr. D. Sekihata, Ms. R. Tanizaki, Mr. Y. Nakazato and Mr. T. Yuasa and other Hiroshima group members. Especially, I had an enjoyable thanks to R.Tanizaki, both in my public and my private life.
I would like to express my thank to the PHENIX collaboration and the PHENIX-J group. They supported my life at BNL and advised in my thesis work.

7 Appendix

7.1 Charged Particle

A charged particle loses kinetic energy, and is deflected the direction when it passes through the material. It mainly interact atoms or electrons in the material. Its process is expressed with Beth-Bloch.

$$-\frac{dE}{dx} = nZz^2\frac{4\pi\alpha^2(hc)^2}{m_e c^2\beta^2}(ln\frac{2m_e c^2\beta^2\gamma^2}{I} - \beta^2) \tag{9}$$

where n is density of atom in the material, Z_e is charge of atoms, m_e is mass of electrons, ze is charge of the particle, I is parameter of average exiting potential ($I \simeq 16Z^{0.9}$eV). As known from this Eq, the energy loss independent mass of the particle, but depend on the speed (β^{-2}) and the charge (z^2). In addition, if particle have same charge, the energy loss is same value in case of increasing the speed ($\beta \geq 0.96$), it is called minimum ionization particles.

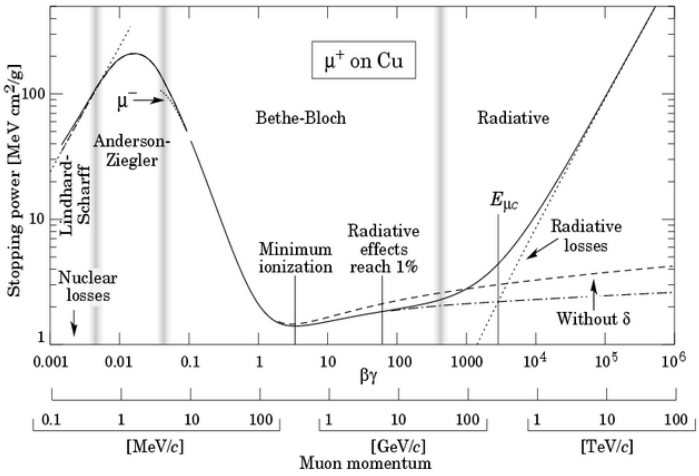

Figure 50: Stopping power for positive muons in cupper [1]

Also low mass particles as electrons and positrons cause bremsstrahlung radiation easily. Bremsstrahlung is electromagnetic radiation produced by deceleration of a charged particle when deflected by another charged particle. A photon is converted when the moving charged particle loses kinetic energy by it, i.e, a photon have the loss energy. It is expressed as Eq.

$$\sigma_{brem} \propto \frac{Z^2\alpha^3}{m^2c^4} \tag{10}$$

The σ_{brem} is a cross section of bremsstrahlung.
$\frac{dE}{dx}$ of bremsstrahlung can be written as

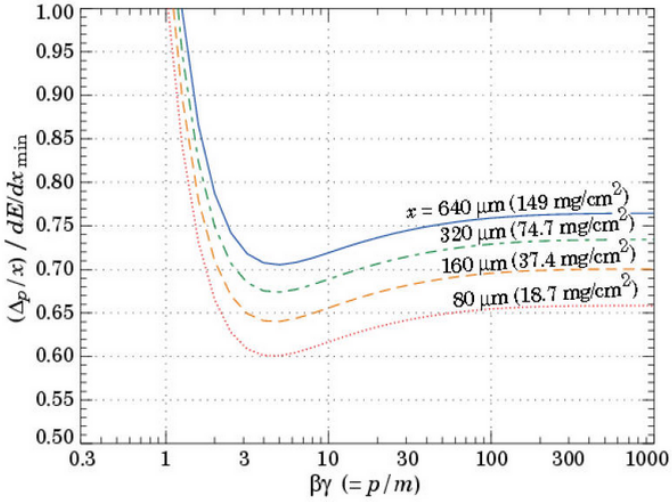

Figure 51: Most probable energy loss in silicon, scaled to the mean loss of a minimum ionizing particle, 388 eV/μm. [1]

$$-\frac{dE}{dx}_r = -\frac{4r_0^2}{137}Z^2E_0Nlog\frac{183}{Z^{1/3}} \tag{11}$$

References

[1] Particle Data Group, *Phys.Rev.D86*,010001 (2012) (//peg.lbl.gov)

[2] K. Yagi *etal.*, *Part.Phys.Nucl.Phys.Cosmol.* 23, 1 (2005) [Quark-Gluon Plasma].

[3] www.bnl.gov/rhic

[4] P. F. Kolb, *HeavyIonPhys.* 21, 234 (2004).

[5] https://www.phenix.bnl.gov/WWW/info/figs/055/

[6] https://www.star.bnl.gov/central/focus/highPt/

[7] David d Enterria *etal.*, High-pT Hadron Suppression and Jet Quenching, $The physics of the Quark - Gluon - Plasma Lecture Notes in Physics$ 785, pp 285-339.

[8] S. Chatrchyan *etal.*, *Phys.Rev.Lett* 109, 222301 (2012) [CMS Collaboration].

[9] http://www.phenix.bnl.gov/plans.html